



HAL
open science

Statistical approach to the Representative Volume Element Size of Random Composites

Dominique Jeulin, Samuel Forest

► **To cite this version:**

Dominique Jeulin, Samuel Forest. Statistical approach to the Representative Volume Element Size of Random Composites. Digital materials, Continuum numerical methods at the mesoscale, In press. hal-03701237v1

HAL Id: hal-03701237

<https://hal.science/hal-03701237v1>

Submitted on 21 Jun 2022 (v1), last revised 18 Jul 2022 (v2)

HAL is a multi-disciplinary open access archive for the deposit and dissemination of scientific research documents, whether they are published or not. The documents may come from teaching and research institutions in France or abroad, or from public or private research centers.

L'archive ouverte pluridisciplinaire **HAL**, est destinée au dépôt et à la diffusion de documents scientifiques de niveau recherche, publiés ou non, émanant des établissements d'enseignement et de recherche français ou étrangers, des laboratoires publics ou privés.

Statistical approach to the Representative Volume Element Size of Random Composites

Dominique JEULIN¹ and Samuel FOREST²

1 Mines Paris, PSL University, Centre de Morphologie Mathématique
dominique.jeulin@minesparis.psl.eu

2 Mines Paris, PSL University, Centre des Matériaux, CNRS UMR 7633,
BP 87, 91003 Evry, France
samuel.forest@minesparis.psl.eu

Apparent properties of random structures may be estimated by homogenization from the numerical solution of the PDE concerning the physical fields on real images or on simulations of random media in bounded domains. For this purpose, numerical calculations are made by Finite Elements or by FFT. This numerical approach involves a statistical definition of a representative volume element RVE to provide intervals of confidence of the estimated apparent properties. For large enough domains, bias errors generated by applied boundary conditions can be neglected. The statistical approach of the RVE is summarized. It is illustrated by examples of application to linear and nonlinear micromechanics, optics, fluid flows and wave propagation, for various types of microstructures of industrial materials, as well as of models of random sets.

Keywords: digital materials, numerical homogenization, apparent elastic moduli, apparent viscoelastic moduli, apparent permittivity, optical properties, acoustic properties, Darcy permeability, viscoplasticity, elastoplasticity, elastoviscoplasticity, hyperelasticity, random set, covariance, integral range, RVE, Finite Elements, Fast Fourier Transform, boundary conditions, Hill-Mandel lemma, Voronoi mosaic, Boolean model, Cox Boolean model, hard-core model, fibrous media, porous media, polycrystals, granular media, nanomaterials

1. Introduction

The usual theoretical prediction of effective properties of random materials concerns media with an infinite extension, modelled by ergodic random structures. On the other hand, more and more 3D digital images of real microstructures become available from efficient observations techniques, such as X-ray microtomography. Images are obtained on large scale instruments like synchrotrons, and even on the laboratory scale, since commercial microtomographs are becoming as usual as SEM. Electron microtomography in the TEM provides images with a much higher magnification, while optical confocal microscopy can be used for this purpose on media transparent to light, as among others biological tissues.

In parallel with these experimental breakthroughs, more and more powerful computational facilities become available, even on desktop computers, making easier to handle very large data sets like 3D images and their processing to improve their quality or to extract objects that they contain.

A faithful representation of microstructures by flexible 3D random models of microstructures, relying on identification of models and of their parameters from partial data or from prior assumptions, can often be obtained with a low computational cost.

Starting from images, efficient numerical solvers and parallel computation techniques allow to get fields as accurate numerical solutions of physical problems driven by PDE, from which apparent physical properties can be estimated by homogenization.

Combining these novelties together, numerical approaches for microstructural physics and mechanics are rapidly expanding in the area of Digital Materials. However, these approaches are irrelevant and questionable if the statistical representativity of the results cannot be mastered. The purpose of this text is to remind through physical examples the principle of numerical computation of apparent properties. This numerical approach involves a statistical definition of a representative volume element RVE to provide intervals of confidence of the estimated apparent properties in the cases of linear and non linear constitutive equations. It is illustrated by examples of application to linear and nonlinear micromechanics, optics, fluid flows and wave propagation, for various types of microstructures of industrial materials, as well as of models of random media.

2. Elements of numerical homogenization of heterogeneous media

2.1. Examples of physical properties of heterogeneous media

Consider a continuum embedded inside a domain (usually bounded) B within the Euclidean space \mathbb{R}^n . In each point x of B , define a set of physical properties $P(x)$ (for instance a stress or strain tensor, a velocity, a temperature, ...). $P(x)$ builds a field defined on the domain B , solution of a problem defined by the following conditions:

- application of conservation principles (for instance momentum, energy) from a local balance involving systems of partial differential equations (PDE). Equilibrium condition imposes that for a given flux $F(x)$,

$$\operatorname{div} F = 0 \tag{1}$$

- appropriate choice of boundary conditions given on the boundaries ∂B of the domain B ;
- use of constitutive equations. For instance, the following linear laws are commonly used:
 - ★ Hooke's law between the stress tensor σ and the strain tensor e in linear elasticity through the fourth rank tensor of elasticity \mathbf{C} :

$$\sigma = \mathbf{C}e \tag{2}$$

- ★ Navier linearised law linking for a fluid the pressure gradient (with components $\partial_i p$) to the Laplacian of the velocity u through the kinematical viscosity μ :

$$\partial_i p = \mu \Delta u_i \tag{3}$$

- ★ Darcy's law between the macroscopic flow rate (with components Q^i) and the macroscopic pressure gradient (with components $\partial_i P$) for a flow in a porous medium, K being the second rank tensor of permeability:

$$Q^i = -\frac{1}{\mu} K^{ij} \partial_j P \tag{4}$$

- ★ For electrostatics of a dielectric medium, proportionality between the electric displacement D and the electric field E , ϵ being the second rank dielectric permittivity tensor, and ϕ the potential:

$$D = \epsilon E = -\epsilon \operatorname{grad} \phi \quad (5)$$

Laws (2-5) are defined for each point x , where only local information is involved in the relations between the variables. For a homogeneous medium, the variables L , μ , K , ϵ (which are positive definite tensors) in equations (2-5) remain uniform in space. The solution to the problem is a field $P(x)$ in B , compatible with the boundary conditions. For the various instances given above, equation (1) is formulated as:

$$\begin{aligned} \operatorname{div} \sigma &= 0 \text{ for continuum mechanics} \\ \operatorname{div}(\operatorname{grad} p) &= 0 \text{ for fluid flows} \\ \operatorname{div} Q &= 0 \text{ for macroscopic flows} \\ \operatorname{div} D &= 0 \text{ for electrostatics} \end{aligned} \quad (6)$$

in the static case and in the absence of source terms.

2.2. Change of scale in heterogeneous media

In the case of linear constitutive equations, existence and uniqueness of the solution for a given geometry are proved, for appropriate boundary conditions. In addition, on a macroscopic scale the same linear constitutive laws apply, with so-called effective properties. More generally, non-linear constitutive equations can be used.

In a heterogeneous medium the constitutive equations can change in space, from:

- different types of constitutive equations (for instance linear for some places and non linear for other places within the domain B);
- variations in space of the coefficients of the equations. They can be modelled either by random functions (Matheron, 1967; Sanchez-Palencia and Zaoui, 1987), or by periodic fields (Sanchez-Palencia and Zaoui, 1987).

In the case of heterogeneous media, the change of scale problem can be formulated as follows:

- Is it possible to replace an heterogeneous medium (with support B) by an equivalent homogeneous medium from a macroscopic point of view?
- If yes, what is the macroscopic constitutive equation and what are the values of its macroscopic coefficients (or effective properties)?

The probabilistic study of the fluctuations of apparent properties estimated in realizations of a random medium in a bounded domain B with possible scale effects is far less advanced. To correctly handle scale depending fluctuations of apparent properties, the notion of statistical representative volume element (RVE) has to be introduced (section 3). Presently this problem can be only studied by numerical methods of simulations on realizations of random media (like among others Finite Elements (FE) (Cailletaud et al., 1994; Kanit et al., 2003, 2006), or Fast Fourier Transform (FFT) (Willot and Jeulin, 2009)).

The interest of change of scale methods is straightforward for applications in material sciences:

- They help to account for the microstructure in the description of the overall behaviour of heterogeneous media. As a result, they can contribute to the optimization of materials. Another important aspect concerns the implementation of constitutive equations on a mesoscale containing microscopic information, for introduction into computation codes used for the design of parts or of structures.
- They connect the microstructure to physical properties of materials useful for their applications. The latter can combine several properties, possibly studied by the same theoretical approach from the single micro-geometrical information.

2.3. Principle of calculation of apparent properties

2.3.1. Definition of apparent properties from space averages

Consider first the case of a vector field, namely the electric field E in a dielectric medium with a real permittivity. The average of any field $P(x)$ in B with volume V is defined as:

$$\langle P \rangle = \frac{1}{V} \int_B P(x) dx \quad (7)$$

For instance the average of the electric field E and of the displacement field D are:

$$\begin{aligned} \langle E \rangle &= \frac{1}{V} \int_B E(x) dx \\ \langle D \rangle &= \frac{1}{V} \int_B D(x) dx = \frac{1}{V} \int_B \epsilon(x) E(x) dx \end{aligned} \quad (8)$$

The apparent dielectric tensor ϵ^* of the equivalent homogeneous medium contained in B is defined in such a way that equation (5) is satisfied on a macroscopic scale:

$$\langle D \rangle = \epsilon^* \langle E \rangle \quad (9)$$

2.3.2. Boundary conditions

In general, ϵ^* depends on the applied boundary conditions on ∂B , on the local permittivity of the components and on the geometry of the medium. The most current applied boundary conditions (BC) are as follows:

- Dirichlet BC: a uniform electric field E_0 is applied on ∂B , or equivalently, introducing the potential $\phi(x)$ so that $E_0 = -\text{grad } \phi$, $\phi(x) = -E_0 \cdot x$, $\forall x \in \partial B$
- Neumann BC: $D \cdot n = D_0$ for $x \in \partial B$ with normal n .
- Periodic BC: $\phi(x) = -E_0 \cdot x + \phi_P(x)$, where $\phi_P(x)$ is a periodic fluctuation, with $\phi_P(x^+) = \phi_P(x^-)$, x^+ and x^- being two homologous points on ∂B . D must be antiperiodic: on two homologous boundaries, $D^+ \cdot n^+ + D^- \cdot n^- = 0$.

Furthermore conditions must be satisfied on the interface between a pair of components. For perfect interfaces, the potential is continuous on the interface, but its normal derivative makes a jump, so that the normal component of E makes a jump on the interface, but its tangential component is continuous. In the remaining parts of this text, the interfaces are assumed to be perfect.

The apparent dielectric tensor can equivalently be defined from the energy $U(x) = \frac{1}{2}E(x)\epsilon(x)E(x) = \frac{1}{2}E(x)D(x)$ (the energy is a quadratic form in the case of a linear constitutive equation, as for linear electrostatics):

$$\langle U \rangle = \frac{1}{2} \langle E \rangle \epsilon^* \langle E \rangle \quad (10)$$

The relations given by equations (8-10) can be applied to any heterogeneous medium in a bounded region B , provided the field $E(x)$ is expressed from the applied boundary conditions and from the partial differential equation expressing the Gauss' law:

$$\operatorname{div} D = \sum_i \frac{\partial}{\partial x_i} (D_i(x)) = 0 \quad (11)$$

This procedure may be used for a periodic medium from the knowledge of the cell building the period (Jikov et al., 1994; Sanchez-Palencia and Zaoui, 1987). When applying periodic BC on the period, or homogeneous BC on a finite domain B the averages of the fields are given by (Jikov et al., 1994; Sanchez-Palencia and Zaoui, 1987):

$$\langle E \rangle = E_0 \quad (12)$$

or

$$\langle D \rangle = D_0 \quad (13)$$

2.3.3. The Hill-Mandel lemma

Starting from the local energy $U(x) = \frac{1}{2}E(x)\epsilon(x)E(x) = \frac{1}{2}E(x)D(x)$ and averaging over the domain B , the following relation is satisfied for the homogeneous or periodic applied boundary conditions to the bounded domain B , from which the apparent dielectric tensor can equivalently be defined (in linear elasticity of heterogeneous media, this result is called the Hill-Mandel lemma for heterogeneous media (Hill, 1963; Kröner, 1972; Sanchez-Palencia and Zaoui, 1987)):

$$\langle U \rangle = \frac{1}{2} \langle ED \rangle = \frac{1}{2} \langle E \rangle \langle D \rangle = \frac{1}{2} \langle E \rangle \epsilon^* \langle E \rangle \quad (14)$$

Equation (14) shows that the random fields E and D are uncorrelated for the homogeneous or periodic applied boundary conditions to the bounded domain B . It holds for any pair (E, D) where $E = -\operatorname{grad} \phi$ and $\operatorname{div}(D) = 0$ satisfying these boundary conditions. This relation is independent on the microstructure contained in a domain B , and does not rely on the linear (or nonlinear) constitutive equation (5) connecting D and E . The Hill-Mandel lemma is the key point for the estimation of the apparent (or effective in an infinite medium) properties and of their fluctuations with the scale of observation, as detailed in section 3.

When a constant electric field E_0 is applied on ∂B , from equation (14) is deduced

$$\langle D \rangle = \epsilon^* E_0 \quad (15)$$

When a constant displacement field D_0 is applied on ∂B , equation (14) yields:

$$\langle E \rangle = (\epsilon^{-1})^* D_0 \quad (16)$$

Therefore, in the case of periodic or of homogeneous BC applied on ∂B , the apparent dielectric permittivity ϵ^* (or the apparent inverse $(\epsilon^{-1})^*$) is obtained from the average $\langle D \rangle$ (or $\langle E \rangle$).

In practice it can be implemented from a numerical solution of the electrostatic problem, knowing the geometry of the medium and the boundary conditions, as will be seen in section 3. Notice that for a bounded domain B in general $(\epsilon^*)^{-1} \neq (\epsilon^{-1})^*$, the equality being obtained asymptotically when $B \rightarrow \mathbb{R}^n$.

If the field $P(x)$ is modelled by an ergodic random multivariate function, for domains B converging to \mathbb{R}^n the spatial averages converge towards mathematical expectations with the following meaning for the variance D^2 :

$$D^2[\langle P \rangle] \rightarrow 0 \text{ when } B \rightarrow \mathbb{R}^n$$

For an ergodic random field of permittivity $\epsilon(x)$ the random field $E(x)$ (and then $D(x) = \epsilon(x)E(x)$) is stationary and ergodic. It can be shown that in these conditions the averages $\langle \cdot \rangle$ in equations (9, 14, 15, 16) become mathematical expectations $E\{\cdot\}$, and the Hill-Mandel lemma can be applied for the infinite random medium (Matheron, 1967, 1968; Jeulin, 2021) (p. 631):

$$E\{D\} = \epsilon^* E\{E\} \tag{17}$$

$$E\{U\} = E\left\{\frac{1}{2}E(x)D(x)\right\} = \frac{1}{2}E\{E\}E\{D\} = \frac{1}{2}E\{E\}\epsilon^* E\{E\}$$

The two definitions of ϵ^* given in equation (17) are then equivalent.

2.3.4. Apparent elastic properties

For the apparent elastic properties of a random medium, a similar approach is made, where the potential is now replaced by the displacement field $u(x)$, the electric field by the deformation field $e(x)$, and D by the stress field $\sigma(x)$. Equation (14) corresponding to the Hill-Mandel lemma becomes:

$$\langle \sigma e \rangle = \langle \sigma \rangle \langle e \rangle \tag{18}$$

Equation (18) holds for any pair (e, σ) where e derives from a displacement field $u(x)$

$$e_{ij}(x) = \frac{1}{2} \left(\frac{\partial u_i}{\partial x_j} + \frac{\partial u_j}{\partial x_i} \right) \tag{19}$$

and $\text{div}(\sigma) = 0$ satisfying boundary conditions given below. It does not rely on the linear constitutive relation (2) connecting σ and e . For micromechanics in a domain B , the common applied boundary conditions (BC) for which the Hill-Mandel lemma is satisfied are as follows (Kanit et al., 2003):

- Dirichlet BC: a uniform deformation e is applied on ∂B , or equivalently $u(x) = e.x$, $\forall x \in \partial B$. It is also called Kinematic Uniform BC (KUBC).
- Neumann BC: for the normal stress components on the boundary ∂B with normal n , $\sigma.n = t$: a uniform traction t is applied on ∂B . This corresponds to Static Uniform BC (SUBC).
- Periodic BC: $u(x) = \bar{e}.x + u_P(x)$, where $u_P(x)$ is a periodic fluctuation vector, with $u_P(x^+) = u_P(x^-)$, x^+ and x^- being to homologous points on ∂B . The traction t must be anti-periodic: on two homologous boundaries, $\sigma^+.n^+ + \sigma^-.n^- = 0$.

As for the electrostatics case, homogenization tools presented in this text are valid for perfect interfaces between components, insuring the continuity of the displacement and of the traction vector components.

2.3.5. Effective and apparent properties in the nonlinear case

The procedure based on the average energy can be extended to nonlinear constitutive equations, for which the function U is not any more quadratic. This happens for instance for elastoplastic porous media, or elastoviscoplastic polycrystals in micromechanics. This is studied by means of variational techniques to work out bounds in (Talbot and Willis, 1985; Ponte Castaneda and Willis, 1988; Willis, 1991, 2001), among others. The definition of apparent properties becomes more difficult in that case, since the average $\langle U \rangle$ or its mathematical expectation $E\{U\}$ can have various expressions as a function of physical properties of the various components A_i of the random medium and of their constitutive equations. In contrast to the linear case, the composition of nonlinear properties by spatial averaging can be more complex. However, in the nonlinear case the expressions (14, 17, 18) resulting from the Hill-Mandel lemma still apply and can be used to compute the macroscopic constitutive equations followed by the random medium. For instance in the case of nonlinear mechanical properties, imposing an average deformation $E\{e\}$, use can be made of the local potential energy $W(x, e)$ and of its space average $\langle W(x, e) \rangle$. For a domain B with infinite extension, the spatial averages of variables are replaced by their mathematical expectations in the ergodic case, so that an effective potential energy W^* is obtained

$$E\{W(x, e)\} = W^*(E\{e\})$$

from which the macroscopic constitutive equation relating $E\{\sigma\}$ to $E\{e\}$ is obtained

$$E\{\sigma\} = \frac{\partial}{\partial E\{e\}} W^*(E\{e\}) \quad (20)$$

Alternatively, when imposing an average stress $E\{\sigma\}$, use can be made of the local complementary energy $U(x, \sigma)$ and of its space average $\langle U(x, \sigma) \rangle$. When $B \rightarrow \mathbb{R}^n$, the spatial averages of variables are replaced by their mathematical expectations, so that an effective energy U^* is obtained

$$E\{U(x, \sigma)\} = U^*(E\{\sigma\})$$

from which the macroscopic constitutive equation relating $E\{e\}$ to $E\{\sigma\}$ is obtained

$$E\{e\} = \frac{\partial}{\partial E\{\sigma\}} U^*(E\{\sigma\}) \quad (21)$$

When using parametric expressions relating $E\{e\}$ and $E\{\sigma\}$ effective material parameters can be estimated. Operating on a bounded domain B , apparent material parameters can be identified from the averages $\langle W(x, e) \rangle$ or $\langle U(x, \sigma) \rangle$, or directly from the curves relating $\langle \sigma \rangle$ and $\langle e \rangle$ obtained by spatial averages of the fields $\sigma(x)$ and $e(x)$ numerically computed from a range of values of applied fields $\langle \sigma \rangle$ or $\langle e \rangle$. Again, these average values (or apparent energies) are subject to statistical fluctuations, which have to be considered in order to provide intervals of confidence of the results of estimation, and to properly define a RVE.

2.4. Homogenization of random media by numerical simulations

An efficient way to solve the problem of homogenization makes use of Digital Materials, and generates numerical solutions of the corresponding partial differential equations, namely the required full fields. In a second step, the effective properties are estimated by spatial averaging of the solution, using the Hill-Mandel condition (Equations (14, 18)). The input

image can be a 3D image of the studied medium obtained by various techniques, like for instance microtomography. When such a 3D reconstruction is not available, use can be made of simulations of realizations of an appropriate model of random structure, after identification from 2D images obtained on sections.

One of the techniques used to solve the homogenization problem is based on the Finite Elements method (FE), as illustrated in (Barbe et al., 2001a). A convenient way to numerically solve the homogenization problem is to use periodic boundary conditions (BC) applied on a periodic cell. For this purpose, simulations of periodic random media were developed, like the Voronoi 3D polycrystal (Decker and Jeulin, 2000). Usually they start from a periodization of the Poisson point process.

Beside the FE method, efficient iterative techniques operating by iterations of Fast Fourier Transform (FFT) on periodic media are available for micromechanics problems (Moulinec and Suquet, 1994), and for electrostatics (Eyre and Milton, 1999). This numerical approach is based on the convolution form of the Lippmann-Schwinger equation (Kröner, 1972), which is easily handled in the Fourier space after Fourier transformation of the involved fields. The main advantages of FFT computations is to avoid a laborious meshing procedure for complex microstructures, as required by the FE method, and to operate with periodic BC which are shown to provide a faster convergence of apparent properties with respect to the volume of numerical simulations (Kanit et al., 2003), as illustrated in subsection 4.1.1. It is directly applied to real or simulated 3D images. Up to 1600^3 images were used to estimate the apparent elastic moduli of granular materials in (Escoda et al., 2016). Moreover, in the case of a two-component random medium, it is possible to handle separately the geometry and the physical properties of the components, so that a single calculation of fields has to be performed, see p. 725-726 in chapter 19 of (Jeulin, 2021). As a consequence, a considerable reduction of the cost of computations can be expected when the impact of the change of contrast of properties, or when one looks for the effect of the frequency ω through $\epsilon(x, \omega)$ in optics or through viscoelastic moduli in viscoelastic materials.

By implementation of such numerical techniques on realizations of models of random media, it is easy to provide parametric studies of the impact on the physical behaviour of realistic microstructures. This provides guidelines towards the design of optimal microstructures with regards to their properties, as was done for instance in the case of ice cream materials (Kanit et al., 2011).

3. Statistical definition of the RVE

When using numerical simulations as defined in subsection 2.4, a question immediately arises: how far are the effective properties estimated on a bounded domain B representative of the full microstructure? In other words, what is the size of a so-called "Representative Volume Element" RVE (Kanit et al., 2003)? Given an estimation of apparent properties obtained from volume averages of computed fields (electric field in electrostatics, stress or strain field in elasticity), what is the statistical interval of confidence of this estimation? A similar question appears for engineering purposes, when working on parts with dimension of the same order as the microstructure; this occurs for instance for some devices like microbeams in microelectronics, where a few grains only are seen across the specimen. In that case the effective properties of different parts (like the elastic moduli of the beam) fluctuate, so that a specific procedure may be required for the quality control in production, with a more or less important amount of rejected parts.

To answer to these questions, higher order statistical information than average values is required, but unfortunately is presently not available from a theoretical calculation without resorting to numerical simulations.

The second order moment of the field in a domain with an infinite extension can be worked out when the effective property is known (Buryachenko and Kreher, 1995; Buryachenko, 2007; Bobeth and Diener, 1986; Kreher, 1990; Kreher and Pompe, 1985; Suquet and Ponte Castaneda, 1993), as detailed in chapter 18 of (Jeulin, 2021), but it does not provide any information on the fluctuations of the average made over a finite domain B . The second moment of the field is obtained by partial derivation of the effective permittivity ϵ^* with respect to the permittivity of phases, starting from equation (17). A first order formal estimation of the variance of the average flow rate in porous media over a finite domain is given by G. Matheron (Matheron, 1967). It is derived from the first order term of the perturbation expansion of the flow rate. Bounds of the variance are worked out in the same reference, for radial flows and specific covariances of the permeability random function.

Developments for the statistical definition of the RVE in numerical homogenization of random media make use of a geostatistical approach based on the experimental determination of the integral range (Matheron, 1971, 1989) from numerical simulations (Cailletaud et al., 1994; Kanit et al., 2003). This is a direct transposition of the approach followed in image analysis of microstructures to give a confidence interval of volume fractions, applied to steels and to iron ore sinters in (Hersant and Jeulin, 1976), and detailed in chapter 3 of (Jeulin, 2021).

3.1. Variance of estimation and integral range

When estimating the average of an ergodic stationary Random Function $Z(x)$ over a domain B with volume V (briefly written $\bar{Z}(V) = \frac{1}{V} \int_V Z(x) dx$) from an average over a domain B' with volume V' ($\bar{Z}(V')$), the obtained result is known with a random error of estimation $\bar{Z}(V) - \bar{Z}(V')$. The variance of this error $\sigma_E^2(V, V')$ is given as a function of the central covariance function $\bar{C}(h)$ of $Z(x)$ by (Matheron, 1965, 1971):

$$\begin{aligned} \sigma_E^2(V, V') &= E \left\{ (\bar{Z}(V) - \bar{Z}(V'))^2 \right\} \\ &= \frac{1}{V^2} \int_B \int_B \bar{C}(x-y) dx dy + \frac{1}{V'^2} \int_{B'} \int_{B'} \bar{C}(x-y) dx dy \\ &\quad - \frac{2}{VV'} \int_B \int_{B'} \bar{C}(x-y) dx dy \end{aligned} \quad (22)$$

where

$$\bar{C}(h) = E\{(Z(x) - E(Z))(Z(x+h) - E(Z))\}$$

In Equation (22), a structural property (through the central covariance) and the geometry of implantation of the fields of measurements (through the domains of integration B and B') are present. In practical applications, simplified expressions can be used (for large domains B and B' , they contain the integral ranges A_n in \mathbb{R}^n), as illustrated for solving sampling problems in image analysis applied to steels and to iron ore sinters in (Hersant and Jeulin, 1976) and below for homogenization. This enables us to define the size of a statistically Representative Volume Element (RVE).

Consider now fluctuations of average values over different realizations of a random medium inside the domain B with the volume V . For an ergodic stationary random function $Z(x)$ with mathematical expectation $E(Z)$, the variance $D_Z^2(V)$ of its average value $\bar{Z}(V)$ in the domain

B of volume V is derived from equation (22) by letting $B' \rightarrow \mathbb{R}^d$ and is given as a function of the central covariance function $\overline{C}(h)$ of $Z(x)$ (Matheron, 1971) by:

$$D_Z^2(B) = \frac{1}{V^2} \int_B \int_B \overline{C}(x-y) dx dy \quad (23)$$

For a large specimen (with $V \gg A_3$), Equation (23) can be asymptotically expressed to the first order in $1/V$ as a function of the integral range in \mathbb{R}^3 , A_3 , by

$$D_Z^2(B) = D_Z^2(V) = D_Z^2 \frac{A_3}{V} \quad (24)$$

$$\text{with } A_3 = \frac{1}{D_Z^2} \int_{\mathbb{R}^3} \overline{C}(h) dh \quad (25)$$

where D_Z^2 is the point variance of $Z(x)$ and A_3 is the integral range of the random function $Z(x)$, defined when the integrals in equations (23) and (25) are finite. When $Z(x)$ is the indicator function of the random set A , equation (24) provides the variance of the local volume fraction (in 3D) as a function of the point variance $D_Z^2 = p(1-p)$, p being the probability for a point x to belong to the random set A . When working in 2D, as was done to solve sampling problems in image analysis (Hersant and Jeulin, 1976), the volume V is replaced by the surface area, and the integral range becomes A_2 after integrating the covariance in \mathbb{R}^2 in equation (25). The asymptotic scaling law (24) is valid for an additive variable Z over the region of interest B and gives a decrease of the variance $D_Z^2(B)$ inversely proportional to its volume V . From equation (24) the volume V is equivalent to $k = \frac{V}{A_3}$ subvolumes in which the average values of the Random Function (RF) $Z(x)$ are uncorrelated random variables. This is why the integral range can be interpreted as a volumetric scale of the microstructure.

Considering now for B a subdomain of B' with volume $V < V'$. For large specimens with $V' > V \gg A_3$, the asymptotic expression of equation (22) becomes:

$$\sigma_E^2(V, V') \simeq D_Z^2 A_3 \left(\frac{1}{V} - \frac{1}{V'} \right) \quad (26)$$

When $V' \gg V$ the term $1/V'$ can be neglected in equation (26) so that equation (24) is recovered. This is usually the case in practice of numerical homogenization.

For infinite integral range the variance $D_Z^2(V)$ decreases more slowly than V^{-1} . From empirical observations, a decrease in $V^{-\gamma}$ with $\gamma < 1$ was proposed (Lantuejoul, 1991). In (Jeulin, 2016) the coefficient γ is theoretically computed in the case of Boolean random varieties (see chapter 6 in (Jeulin, 2021)). When $A_3 = 0$, the decrease of $D_Z^2(V)$ is much faster than V^{-1} , which induces a fast convergence of $Z(V)$ towards its expected value.

Equations (24) or (26) give access to an experimental estimation of the integral range by plotting the curve $D_Z^2(V)$ obtained for different sizes of samples, without the knowledge of the theoretical or of the experimental covariance $\overline{C}(h)$ (Matheron, 1989; Lantuejoul, 1991). This multiscale method of estimation of the integral range is much more robust than using a numerical integration of the experimental covariance, often subject to uncontrolled spurious oscillations around its sill. Its equivalent form when using a $V^{-\gamma}$ scaling gives access to γ and to a test of the validity of the scaling law (Kanit et al., 2003).

3.2. Definition of the statistical RVE of apparent properties

To estimate the effective dielectric permittivity ϵ^* by homogenization from equations (15) and (16), it is required to compute the averages $\langle D \rangle$ or $\langle E \rangle$ in domain B :

$$\langle D \rangle = \frac{1}{V} \int_B D(x) dx = \frac{1}{V} \int_B \epsilon(x) E(x) dx = \langle \epsilon E \rangle$$

For an appropriate choice of the constant electric field E_0 applied on ∂B (namely of the constant displacement field D_0) and in the isotropic case, ϵ^* is obtained from the estimations of a single component of $\langle D \rangle$ or $\langle E \rangle$. Therefore the variance of the apparent property ϵ^* (it would be the effective property for $B \rightarrow \mathbb{R}^n$) follows equations (24) or (26) when the integral range A_3 of the relevant field is known. This requires the stationarity of the fields D and E , obtained for appropriate boundary conditions (homogeneous or periodic, as seen in section 2.3.1). A similar approach can be used when the local (or even the global) permittivity is described by a tensor, but numerical simulations must be done with various vectors D_0 or E_0 applied on ∂B . This approach is exactly the same as in the case of elastic properties of a random medium and was introduced from numerical simulations in 2D in (Cailletaud et al., 1994). To be valid, the approach giving the variance of estimation of $\bar{Z}(V)$ based on equations (24) or (26) requires the stationarity and the ergodicity of the fields (E , D , or e , σ). This is satisfied for any infinite random medium with stationary and ergodic moduli see (Jeulin, 2001) and (Jeulin, 2021), p. 629-630. Large efforts have been recently made to prove the $1/V$ scaling of the variance of estimation corresponding to equation (24) by involving some Central Limit Theorem proved only for some specific random fields of coefficients like the dielectric permittivity $\epsilon(x)$ (see (Armstrong et al., 2019; Egloffé et al., 2015; Gloria et al., 2015; Duerinckx et al., 2020), and the references quoted therein, among others). In fact the general geostatistical approach does not need such restrictions.

Since the theoretical or the experimental covariance of the fields (E , D , or e , σ) is usually not available, the integral range can be estimated in the case of homogenization according to the procedure proposed by G. Matheron for any random function (Matheron, 1989): working with multiple realizations on domain a B with an increasing volume V , the parameter A_3 is estimated by fitting the obtained empirical variance according to the expression (24). Alternatively, considering now average values in subdomains B_i with a wide range of sizes, or simulations in a large domain B' , the parameter A_3 is estimated by fitting the obtained variance according to the expression (24) or (26) for volume $V \gg A_3$ where this expression is satisfied. This parameter does not depend on V , provided it is large enough to ensure the stationarity of the field by minimizing the effect of boundary conditions. A first application of this methodology to elastic fields was developed in (Cailletaud et al., 1994).

The point variance of the concerned field is directly estimated from its calculated map. In early studies on the statistical RVE, and even still in some recent papers, the point variance was estimated from the corresponding point variance of a given property. For instance in the case of a two phase composite with a scalar property Z_1 for phase 1 (with the volume fraction p), and Z_2 for phase 2, the point variance D_Z^2 of the random variable Z is given by :

$$D_Z^2 = p(1-p)(Z_1 - Z_2)^2 \quad (27)$$

However the value D_Z^2 given in equation (27) is a rough estimate of the required point variance correctly deduced from the corresponding field, as illustrated in section 4.3.1. Furthermore for an infinite contrast obtained when $Z_1 \rightarrow \infty$, D_Z^2 given by equation (27) goes to infinity and the empirical estimation of the integral range would give a zero value, which is non-physical.

Some typical microstructures with long range correlations, like dilated Poisson hyperplanes or dilated Poisson lines in 3D studied in chapter 6 of (Jeulin, 2021), have an infinite integral range (Jeulin, 1991b,a), so that the computation of the variance $D_Z^2(V)$ of equation (24) cannot be used any more. In this situation, a scaling power law with an exponent $\gamma < 1$ was suggested (Lantuejoul, 1991), and used in various applications, where a coefficient close to 1 was empirically estimated (Cailletaud et al., 1994; Kanit et al., 2003). With this scaling law, the variance becomes

$$D_Z^2(V) = D_Z^2 \left(\frac{A_3}{V} \right)^\gamma, \quad (28)$$

where the volume A_3 is no more the integral of the central covariance function $\overline{C}(h)$, but is still homogeneous to a microstructural volume. In practice, the effect of the volume of samples given by equation (24) is correct for a restricted range of volumes (the largest ones), as a result of its asymptotic character. This has to be checked on data. In addition, the perturbation of boundaries when imposing homogeneous boundary conditions introduces a lack of stationarity which is more sensitive at small scale, and may induce some spurious power law of the variance (with $\gamma < 1$) on a small scale, according to equation (24). Again this has to be carefully checked in every situation, as it is done in the references.

3.3. Practical determination of the size of the RVE

The size of a RVE can be defined for a physical property Z , a contrast, and a given precision in the estimation of the effective properties depending on the number n of realizations that are available. By means of a standard statistical approach, the absolute error ϵ_{abs} and the relative error ϵ_{rela} on the mean value $E\{Z\}$ obtained with n independent realizations of volume V are deduced from the 95% interval of confidence by:

$$\epsilon_{abs} = \frac{2D_Z(V)}{\sqrt{n}}; \quad \epsilon_{rela} = \frac{\epsilon_{abs}}{E\{Z\}} = \frac{2D_Z(V)}{E\{Z\}\sqrt{n}}. \quad (29)$$

The size of the RVE can now conventionally be defined as the volume for which for instance $n = 1$ realization (as a result of an ergodicity assumption on the microstructure) is sufficient to estimate the mean property $E\{Z\}$ with a relative error (for instance $\epsilon_{rela} = 1\%$), provided the variance $D_Z^2(V)$ is known from the asymptotic scaling law (24), (26) or (28). Alternatively, it can be decided to operate on smaller volumes (provided no bias is introduced by the edge effect resulting from the boundary conditions), and to consider n realizations to obtain the same relative error. It is noticed from extensive results of numerical simulations in (Kanit et al., 2003) that the mean value given by the periodic boundary conditions varies slightly as a function of the size of the domain, as compared to the other boundary conditions (SUBC or KUBC). This more or less significant bias, due to the effect of the boundaries ∂B , is found in the mean value given by all boundary conditions for small volume sizes, the value being different from the effective one obtained for large specimens, so that the scaling law (24) must be applied with some caution. For small volumes, the average moduli obtained by simulations depend on the boundary conditions: for instance, in the case of the dielectric permittivity, imposing E_0 on ∂B produces results close to the upper Wiener bound, while imposing D_0 on ∂B gives results close to the lower Wiener bound. This bias is well-known (Huet, 1990; Ostoja-Starzewski, 1998; Sab, 1992), and corresponds to the case of the two homogeneous trial fields from which these bounds are derived. It must be taken into account for the definition of

the RVE. The result is that the mean value computed on too small specimens cannot represent the effective response for the composite material even using the periodic boundary conditions and a sufficient number of realizations. From simulations given in (Kanit et al., 2003) and summarized below in subsection 4.1.1, it appears also that the mean value obtained with the periodic BC is unbiased for smaller sizes of B than for the other BC, but it leads in general to higher variances than for the two other conditions, requiring a larger number of simulations to get a given precision for the effective property. The scaling with volume V of the error resulting from the bias is briefly introduced in subsection 3.4.

3.4. Scaling of the bias, or systematic error

The boundary conditions applied to the domain B in \mathbb{R}^3 with volume V and surface area S may introduce a bias in the estimated apparent properties. It is due to an edge effect produced by a boundary layer with thickness t where the applied fields differ from the fields acting inside B : instead of $Z(x)$ the numerical simulation provides in each point x the value $Z(x) + Y(x)$, $Y(x)$ being the local systematic error. This boundary layer is mentioned in early papers on homogenization of random media for the case of the electric field in electrostatics (Beran, 1965) and for elastic fields in micromechanics, among others (Beran and McCoy, 1970), (Kröner, 1972) p. 108, (Willis, 1982). In usual homogenization of random media, domains B with infinite extension are considered, so that the impact of boundary conditions is eliminated. In the case of finite domains B , boundaries must be accounted for. It is easy to work out a scaling law of the bias when assuming that the systematic error $Y(x)$ is localized in a small domain δB inside B (with average \bar{Y} in δB), close to the boundary ∂B , so that $Y(x) = 0$ when $x \in B \cap \delta B^c$. When estimating $E(Z)$ by the volume average of $Z(x)$, the overall error of the estimation is given by:

$$\begin{aligned} \langle Z + Y \rangle - E(Z) &= \frac{1}{V} \int_B (Z(x) + Y(x)) dx - E(Z) \\ &= \langle Z \rangle - E(Z) + \frac{1}{V} \int_{\delta B} Y(x) dx \\ &= \langle Z \rangle - E(Z) + \frac{1}{V} \bar{Y} t S \end{aligned}$$

From the above expression of $\langle Z + Y \rangle - E(Z)$ the variance of the overall error is given by

$$\begin{aligned} &E\{(\langle Z + Y \rangle - E(Z))^2\} \\ &= D^2(Z) + \frac{1}{V^2} E\{(\bar{Y} t S)^2\} + \frac{2}{V^2} E\{(\langle Z \rangle - E(Z)) \frac{1}{V} \int_{\delta B} Y(x) dx\} \\ &= D^2(Z) + \frac{S^2}{V^2} t^2 E\{(\bar{Y})^2\} \end{aligned}$$

neglecting the correlation between fields $Z(x)$ and $Y(x)$ inside δB ; as far as we know, this is implicitly assumed in published papers about the scaling of the systematic error.

The variance of the overall error is the sum of two terms, namely the usual variance of the statistical error $D^2(Z)$ and the second order moment of the bias (error due to the boundary layer). Therefore the contribution of the bias to the variance scales as $V^{-\frac{2}{3}}$ (or L^{-2}) if L is a measure of the size of B . As an immediate result, the contribution of the bias to the standard deviation scales as $V^{-\frac{1}{3}}$ (or L^{-1}). For homogenization in \mathbb{R}^2 the same L^{-2} scaling is expected after introduction of a boundary layer close to the perimeter of B . The pre-factor $t^2 E\{(\bar{Y})^2\}$

due to the bias depends on the boundary conditions and on the scale of the random function $Z(x)$. It is difficult or even impossible to obtain its value in a closed form, in contrast with the pre-factor of the variance of the random error given in equation (24). It is easy to deduce a similar scaling law for the absolute systematic error defined by (see for instance (Schneider et al., 2022)):

$$\begin{aligned} |E\{\langle Z + Y \rangle\} - E(Z)| &= |E\{\langle Y \rangle\}| = \frac{1}{V} E\left\{ \left| \int_{\delta B} Y(x) dx \right| \right\} \\ &= \frac{1}{V} tSE\{|\bar{Y}|\} \end{aligned}$$

and the same scaling as for the standard deviation of the error is recovered, with the same difficulty to recover the pre-factor $tE\{|\bar{Y}|\}$ in general.

Considerable efforts have been recently made in the so-called "Stochastic Homogenization" community to provide theoretical results on the scaling of the variance $D^2(Z)$ and of the absolute systematic error. In (Egloffé et al., 2015) the L^{-1} scaling of the absolute systematic error is conjectured with the same boundary layer argument. It is successfully tested by numerical simulations in the discrete case of independent random conductivities in \mathbb{Z}^2 and \mathbb{Z}^3 and with Dirichlet boundary conditions. Additional theoretical results are obtained in the discrete periodic case with independent random conductivities (Gloria et al., 2015; Duerinckx et al., 2020), where the following scaling of the absolute systematic error is given in \mathbb{Z}^d by:

$$|E\{\langle Z + Y \rangle\} - E(Z)| \lesssim L^{-d} \ln^d L \quad (30)$$

From this scaling of the error, a higher efficiency of the periodic version of random media is expected for homogenization. However, the degree of generality of this result, in particular concerning the structure of random media for which it can be applied, is presently unknown. Periodic simulations with independent random conductivities in \mathbb{Z}^2 and a low contrast equal to 4 (Egloffé et al., 2015) do follow the scaling law given by equation (30), but the standard L^{-1} scaling is observed for periodic media with a non zero correlation length. In all cases, the average absolute systematic error was observed to be much smaller than the random error.

Simulations of non overlapping objects (spheres and fibres in \mathbb{R}^3 and discs in \mathbb{R}^2) in (Schneider et al., 2022) are used to estimate the thermal conductivity of random media with a low contrast equal to 6. For spheres and for discs, the average absolute systematic error (estimated by considering the estimation of simulations of the largest sample as the true effective conductivity) seems to scale as $V^{-\frac{1}{3}}$ (or L^{-1}) for the periodic and for the standard geometry, as seen from Figures 7 and 9 of this paper. For short fibres the L^{-1} scaling is observed in the standard case, while a possible L^{-2} scaling (dropping the logarithmic term in equation 30) is obtained for the periodic case of Figure 12, but this last conclusion is derived from 3 sizes of simulations only, which is not very reliable. The data given in this paper are obtained on a very small range of scales (a factor limited to 16 for spheres, 32 for discs and 2 for fibres), so that the observations should be confirmed on a much wider range of scales, but apparently the L^{-1} scaling seems to be dominant for these more realistic microstructures than a discrete set of independent conductivities. In the simulations of (Schneider et al., 2022), the average absolute systematic error is lower by an order of magnitude for the periodic case, and is lower than the random error (with an order of magnitude for spheres and for discs); for fibres, the systematic error and the random error are similar, showing a higher sensitivity to artefacts introduced by edge effects. From the available results, for large enough simulations the bias generated by boundaries can be neglected, as made in most available statistical approaches of the RVE.

3.5. Determination of the size of the RVE in the nonlinear case

In the nonlinear case it is wise to start from the apparent energy defined in subsection 2.3.5 for which the same approach as for the linear case can be followed: in micromechanics, for each set of applied conditions $\langle \sigma \rangle$ or $\langle e \rangle$ the variance of the average $\langle W(x, e) \rangle$ or $\langle U(x, \sigma) \rangle$ can be estimated, from which an integral range and the size of the RVE can be obtained. Consider for instance the potential energy $W(x, e)$ and its expectation $W^*(E\{e\})$:

$$2W(x, e) = \sigma(x)e(x)$$

From the Hill-Mandel lemma,

$$2\langle W(x, e) \rangle = \langle \sigma e \rangle = \langle \sigma \rangle \langle e \rangle$$

so that for a given $\langle e \rangle$ the variance of $\langle W(x, e) \rangle$ is proportional to the variance of $\langle \sigma \rangle$. Therefore the determination of the size of the RVE in the nonlinear case is directly derived from the size of the RVE of the field $\sigma(x)$. This should be preferred to any statistical analysis of the parameters of the constitutive law obtained on a small scale, for which the point variance, and as a result the integral range, is not properly defined by equation (27).

3.6. Remarks on the reduction of variance

When using simulations of a random microstructure, some authors of recent publications try to get rid of fluctuations by fixing some parameters for each realization, like for instance the volume fraction of components, or even other morphological properties like set covariances or higher order moments, defining a so-called "representative unit cell" (Matouš et al., 2017). Sometimes the volume fraction is constrained to a unique value whatever the scale of observation. This naive approach is proposed to reduce the variance of estimation of properties and of homogenized coefficients, in order to limit the number of simulations. Needless to say that such a procedure may be the source of uncontrolled biases, the effective behaviour depending non-linearly on such parameters like volume fractions or higher order morphological properties. Hoping to be able to make a correct macroscopic prediction with a single small representative realization satisfying some constraints is a methodology very close to the traditional approaches considering a single RVE to represent the microstructure. Unless ergodicity conditions are reached by means of a single large enough simulation (which can be checked through the estimation of integral ranges), there is no warranty on the quality of the prediction, due to some uncontrolled features, or due to the generation of bias by the effect of some BC, as illustrated by some of the studies presented later. Moreover, such an approach is non-physical and generates mathematical inconsistencies when working on random media: on one hand, fixing the volume fraction of a composite on samples B with volume V is equivalent to constrain $A_3 = 0$ from equations (26), (24). On the other hand, considering random subvolumes of B , fluctuations of local volume fractions are automatically generated, from which a non zero integral range can be estimated. It is difficult to predict the impact of such a contradiction on the predicted effective properties, more specifically for a large contrast of properties of various constituents. In this context, it is preferable to avoid any attempt of reduction of the variance.

4. Examples of application

In this section the methodology developed to estimate the size of the statistical RVE is illustrated in various situations covering a wide range of applications. An exhaustive review of

applications of the statistical RVE is not possible, since the first published work on this tool (Kanit et al., 2003) is currently mentioned in more than 2000 publications. That is why we will limit our purpose to some significant applications. More details for each example are given in the references and in (Jeulin, 2021), chapter 19.

4.1. Linear elastic properties and thermal conductivity

4.1.1. Two-components media on the Voronoi mosaic

In a pioneering work (Kanit et al., 2003) followed by many applications published these last twenty years, the fluctuations of apparent elastic properties and thermal conductivity are studied from finite element simulations. A two-components model is obtained from a random Voronoi mosaic (Figure 1): starting from a random Voronoi tessellations of the 3D space, every cell of the tessellation is randomly and independently affected to component 1 with the probability p and to component 2 with the probability $1 - p$. By convention, cells C have here a unit average volume $E\{V(C)\}$, so that the volume of each simulation is of the order of the number of cells that it contains. Simulations are made for two values of p (and consequently of the volume fraction): $p = 0.5$ and $p = 0.7$. For any random mosaic medium in \mathbb{R}^3 the integral range A_3 does not depend on p and is given by

$$A_3 = \frac{E\{(V(C))^2\}}{E\{V(C)\}} \quad (31)$$

Simulations of periodic random media are used from the periodic version of the Voronoi tessellations (Decker and Jeulin, 2000). Most calculations of apparent properties are made for a contrast $c = 100$ of the Young's moduli and of the thermal conductivities, the larger property being chosen with the probability p . Three types of boundary conditions are investigated: KUBC, SUBC and periodic for elastic moduli; uniform temperature gradient UGT (or Dirichlet), uniform heat flux UHF (or Neumann) and periodic for the thermal conductivity. The main results are summarized as follows:

- The size effect given by equation (23) for the variance $D_Z^2(V)$ is recovered for the local volume fraction, while the size effect given by equation (28) is observed for apparent elastic moduli (bulk and shear moduli) and thermal conductivity, with a coefficient $\gamma \simeq 1$. The estimated value of the integral range from empirical variances obtained for $p = 0.5$ and $p = 0.7$ are equal to 1.178 and 1.111, in agreement with its theoretical value (here $A_3 = 1.179$), which validates the simulations and the procedure of estimation of A_3 from the data $D_Z^2(V)$.
- It is observed that the integral range of apparent properties (elastic moduli and thermal conductivity), deduced from a point variance calculated from equation (27), depends on the property of interest and on its contrast over the two components. It is of the order of twice the integral range of the volume fraction for the Voronoi mosaic, but this result cannot be generalized to any microstructure or physical property.
- Small sizes of realizations introduce a bias of apparent properties, as illustrated by Figures 2 and 3 in the case of the apparent bulk and shear moduli K and G . This bias is much higher for KUBC and SUBC (it disappears for volumes containing at least 1000 Voronoi cells in the case of elastic moduli) than for periodic boundary conditions (the bias disappears for volumes containing at least 15 cells). Similarly the bias is higher for UGT and UHF, where at least 100 cells are required for unbiased simulations, than for periodic boundary conditions, requiring at least 15 cells.

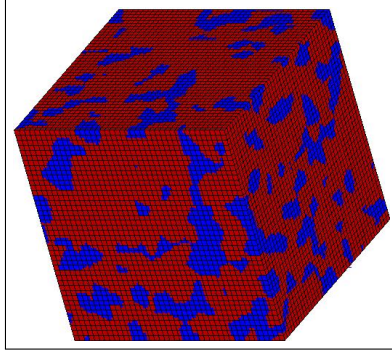


Figure 1: Realization of a two-components Voronoi mosaic, with the FE mesh (Kanit et al., 2003)

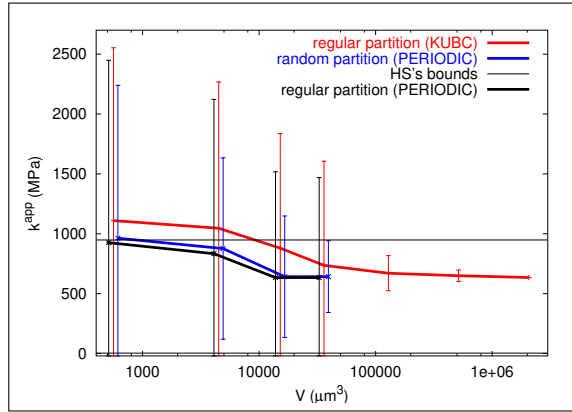


Figure 2: Apparent bulk modulus K and interval of variation estimated from FE calculation with different BC and volumes V for the Voronoi mosaic with $p = 0.7$ (Kanit et al., 2003)

- The variance of apparent properties is always larger for periodic boundary conditions, requiring more realizations for a given statistical precision of the apparent properties, but smaller volumes can be used in simulations. Typically, about 1700 realizations of domains containing in average 15 cells were shown to be used to estimate the elastic moduli with a relative precision $\epsilon_{rela} = 5\%$ in the case of $p = 0.7$ and $c = 100$.

4.1.2. Materials from food industry

The previous methodology was applied for the first time to real 3D images of two materials from food industry, namely ice creams, obtained by optical sectioning with a confocal microscope (Kanit et al., 2006). The purpose was to explain from numerical calculations the different apparent properties observed for the two materials in the presence of two components with a high contrast (1000 for Young's moduli and 100 for thermal conductivities), so that standard bounds are far apart and therefore inefficient to give estimates of the effective properties. The harder phase covers 70% of the volume, and a factor two is observed for the experimental Young's moduli of the two materials.

Numerical simulations of elastic and thermal fields are made by finite elements with the three types of boundary conditions, KUBC, SUBC, and periodic for elasticity; UGT, UHF and periodic for thermal properties.

Having a single volume image for each material, the only way to use a statistical approach of the RVE is to cut subvolumes of various sizes, either by partitioning the image, or taking

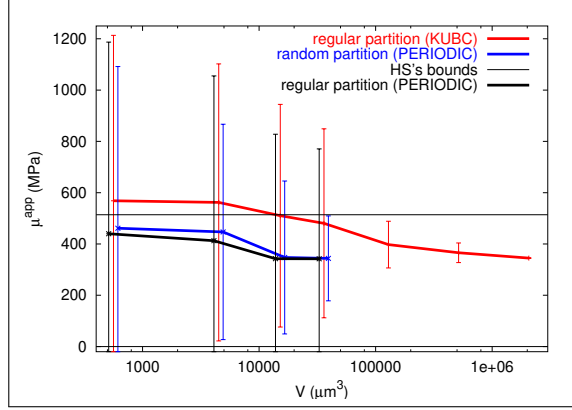


Figure 3: Apparent shear modulus G and interval of variation estimated from FE calculation with different BC and volumes V for the Voronoi mosaic with $p = 0.7$ (Kanit et al., 2003)

random subvolumes. It illustrates the efficiency of the statistical RVE approach, which can be operated for a single large realization of the microstructure. Here are the main results:

- To avoid bias in the estimation of apparent properties, volumes larger than $(24\mu m)^3 = 13824\mu m^3$ are required for periodic boundary conditions. Periodic boundary conditions are applied even if the microstructure is not periodic.
- The integral ranges of the properties are larger for the material with a coarser microstructure, as expected.
- The largest integral range of the elastic moduli is found for the shear modulus, resulting from the fact that the contrast in shear modulus between the two components is higher than for the bulk modulus.
- The integral range corresponding to the thermal conductivity is much higher (factor 2 to 4) than for elastic fields, resulting in this case in larger sizes of RVE.
- The investigated volume of the material with the finer microstructure is sufficient to provide apparent Young's modulus with a correct precision ($\epsilon_{rela} \simeq 15\%$ and 6%), but three equivalent volumes should be used to reach $\epsilon_{rela} \simeq 5\%$, requiring the input of more images.

4.1.3. Unidirectional fibre composite by finite elements

A unidirectional composite with a PA6 matrix and long parallel glass fibres is studied in (Oumarou et al., 2011). Image analysis and FE element calculations of thermal and elastic fields are made on transverse sections, where fibres are displayed as non-overlapping discs with heterogeneous locations, mainly due to the presence of plies in the manufacturing process. The average volume fraction is 0.4, and the average fibre diameter $16\mu m$. The RVE is estimated for all properties of the composite. The most sensitive property to fluctuations of the microstructure is the transverse shear modulus, for which the RVE size is the largest: for a square image with $854\mu m$ edge, containing about 1310 fibres, its relative precision is 18.7% for a single image, and therefore 1.87% for 100 images.

4.1.4. Random fibre composites by iterations of FFT

In (Altendorf et al., 2014) microtomographic images and 3D simulations of various random networks of finite fibres having a length of the order of the size of the samples, various distributions of fibre orientation and radius, are generated with the volume fraction $V_V \simeq 0.15$ to predict the elastic properties and the conductivity by iterations of FFT.

A glass-fibre reinforced polymer is examined by microtomography with a voxel sampling of $3.5\mu m$. After application of a segmentation procedure to separate fibres, length-weighted radius and orientation distributions are estimated from 3D images. Estimated curvature parameters are introduced as input in a random-walk-based model of three-dimensional fibre systems to generate virtual fibrous media with controlled bending of fibres (Altendorf and Jeulin, 2011).

Various types of generated periodic microstructures range from isotropic to transversely isotropic, and to orthotropic media, representing plausible virtual fibrous materials for fibres with average length $1.19mm$ (or equivalently 340 voxels). The anisotropy of the macroscopic responses and the size of the corresponding representative volume element (RVE) are examined numerically. Field calculations are made by FFT on simulations with typical size 600^3 voxels. The elastic and thermal properties of the system studied in (Oumarou et al., 2011) are used for comparison.

It is found that the variance of the properties on a volume V scales as a power law $\sim 1/V^\gamma$ with $\gamma < 1$ and in the range $0.71 - 0.87$, in agreement with equation (28). This is a consequence of the long-range correlations in the microstructure, in comparison to the size of simulations, resulting in a slower decrease of the variance of local averages as usual, but faster than for the Poisson fibres where $\gamma = 2/3$, as seen in section 4.1.5. Concerning the RVE size, a relative precision in the range $0.29 - 1.86\%$ is reached with 10 realizations in cubic domains with 400^3 voxels for the full set of parameters of interest: fibre volume fraction V_V , elastic moduli and thermal conductivity for all considered fibrous systems. Lower size volumes can be used from flat specimens accounting for the main orientations of the fibrous system.

4.1.5. Examples of random media with infinite integral range: Poisson fibres and gigantic RVE

A family of random media with infinite integral range is constructed as follows: by dilation of Poisson varieties V_k of dimension $k < n$ (Matheron, 1975), various Boolean varieties are generated in the space with dimension n , \mathbb{R}^n (Jeulin, 1991b,a, 2016). Consider a convex domain K in \mathbb{R}^n , with Lebesgue measure (volume in 3D) $\mu_n(K)$. The scaling law of the variance of the volume fraction given by equation (28) is theoretically obtained for the Boolean model built on isotropic Poisson varieties V_k (Jeulin, 2016): in \mathbb{R}^n , the theoretical expression of the variance $D_Z^2(K)$ of the local fraction $Z = \frac{\mu_n(A \cap K)}{\mu_n(K)}$ of a Boolean model built on isotropic Poisson varieties of dimension k ($k = 0, 1, \dots, n - 1$) V_k , is expressed as

$$D_Z^2(K) = p(1 - p) \left(\frac{A_k}{\mu_n(K)} \right)^{\frac{n-k}{n}} \quad (32)$$

the scaling exponent being $\gamma = \frac{n-k}{n}$. As particular cases, Poisson points ($k = 0$) give the standard Boolean model with a finite integral range and $\gamma = 1$, Poisson lines ($k = 1$) generate Poisson fibres with $\gamma = \frac{n-1}{n}$, and Poisson hyperplanes ($k = n - 1$) provide Poisson strata with $\gamma = \frac{1}{n}$. It turns out that the most penalizing situation with respect to the scaling of the variance is the case of Poisson strata, with a very slow decrease of the variance with the volume of the sample K , where $\gamma = \frac{1}{n}$. For isotropic Boolean fibres in 2D, the scaling exponent is $\gamma = \frac{1}{2}$

(working in 2D, dilated Poisson lines were used to model a fibre network (Delisée et al., 2001)). For isotropic Boolean fibres in 3D, the scaling exponent is $\gamma = \frac{2}{3}$. For isotropic Boolean strata in 3D, the scaling exponent is $\gamma = \frac{1}{3}$. This decrease of the variance with size is much slower than the case of a finite integral range. When considering random media with a nonlinear behaviour, like for instance a viscoplastic material, a strong localization of strains resulting in shear bands is expected. This generates long range correlations of the fields, that might be modelled by Boolean strata in 3D, and scaling laws similar to the dilated Poisson hyperplanes (with a scaling exponent close to $\frac{1}{3}$) might be recovered, so that a slow convergence towards the effective properties should be observed on numerical simulations with increasing sizes (Jeulin, 2012). This point remains to be investigated by numerical experiments.

The theoretical and observed scaling laws of the variance for fibrous media made of long fibres at the scale of simulations make difficult the statistical convergence of apparent properties to the effective properties, that requires much larger RVE or much more realizations than the standard case. In addition, Poisson fibres (or Poisson strata) with infinite length cannot be periodized (any attempt to make them periodic would completely cover space...), which makes numerical homogenization a challenge in these situations, despite their practical interest for some types of materials.

Simulations for the estimation by finite elements (Dirrenberger et al., 2014) of the elastic properties and of the conductivity of 3D random Poisson fibres (illustrated on Figure 4) surrounded by voids provide an empirical scaling law of the variance close to the theoretical one obtained for the volume fraction. This is expected, as a result of a high correlation between the elastic or thermal fields and the indicator function of the random set A .

Thermal conductivity λ and elastic properties are estimated over hundreds of realizations, with up to 800 fibres for the largest fields. The average measured fibre volume fraction is $p = 0.162 \pm 0.013$. The convergence of λ^{app} is reached for a volume $V = 10^3$ containing nearly 180 fibres. The relative discrepancy error on the mean value of λ^{app} between UTG and MTBC (Mixed thermal BC satisfying the Hill-Mandel lemma, detailed in (Dirrenberger et al., 2014)) is about 16% for the largest sample. There is a strong discrepancy between the KUBC and MBC (mixed tri-axial loading detailed in (Dirrenberger et al., 2014)) estimates K^{app} and G^{app} for largest volumes, showing a lack of convergence of apparent elastic properties due to insufficient volumes. The variance of all measured parameters decreases slowly with the volume V , according to equation (28) with $\gamma = 2/3$, as theoretically predicted for the fibre volume fraction. It is illustrated for K^{app} on Figure 5. Calculation of the statistical relative precision obtained from the simulations show that they are in the range 2.3 – 7.1%. Reaching a 5% relative precision with a single realization would require much larger volumes than used in the present numerical simulations, from 164^3 to 489^3 , depending on the property and on the BC.

4.1.6. Anisotropic elasticity in bulk polycrystals and thin films

The statistical approach to RVE size is applied to the effective elastic bulk properties of metallic polycrystals by (El Houdaigui et al., 2007a). The example deals with a Voronoi tessellation of copper grains as shown in Figure 6. A uniform distribution of crystal lattice orientations is attributed to the grains of the volume element. Copper single crystals exhibit cubic anisotropy and three independent elastic moduli are:

$$C_{11} = 168000 \text{ MPa}, \quad C_{12} = 121400 \text{ MPa}, \quad C_{44} = 75390 \text{ MPa}$$

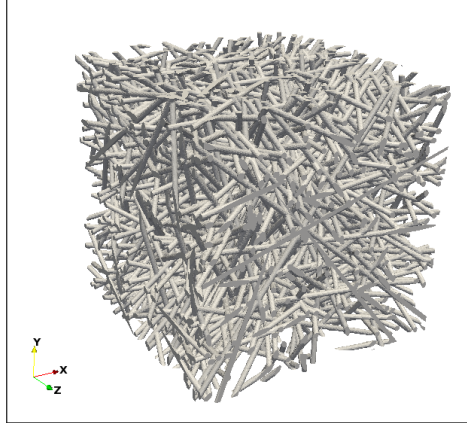


Figure 4: 3D simulation of Poisson fibres (radius 1 in a cube with edge 60) (Dirrenberger et al., 2014)

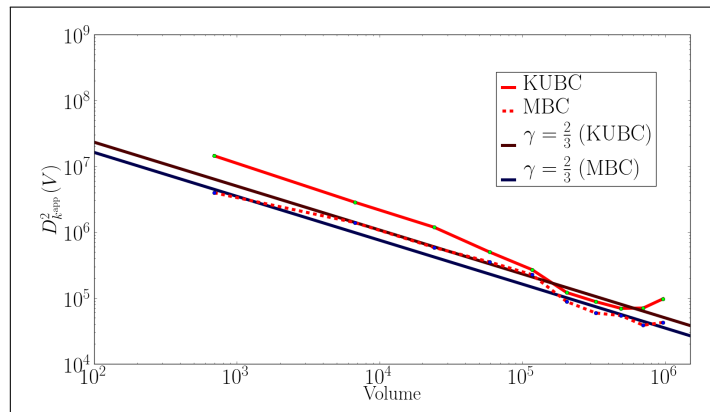


Figure 5: Variance scaling of the apparent bulk modulus K^{app} with the volume of simulations (logarithmic scales) (Dirrenberger et al., 2014)

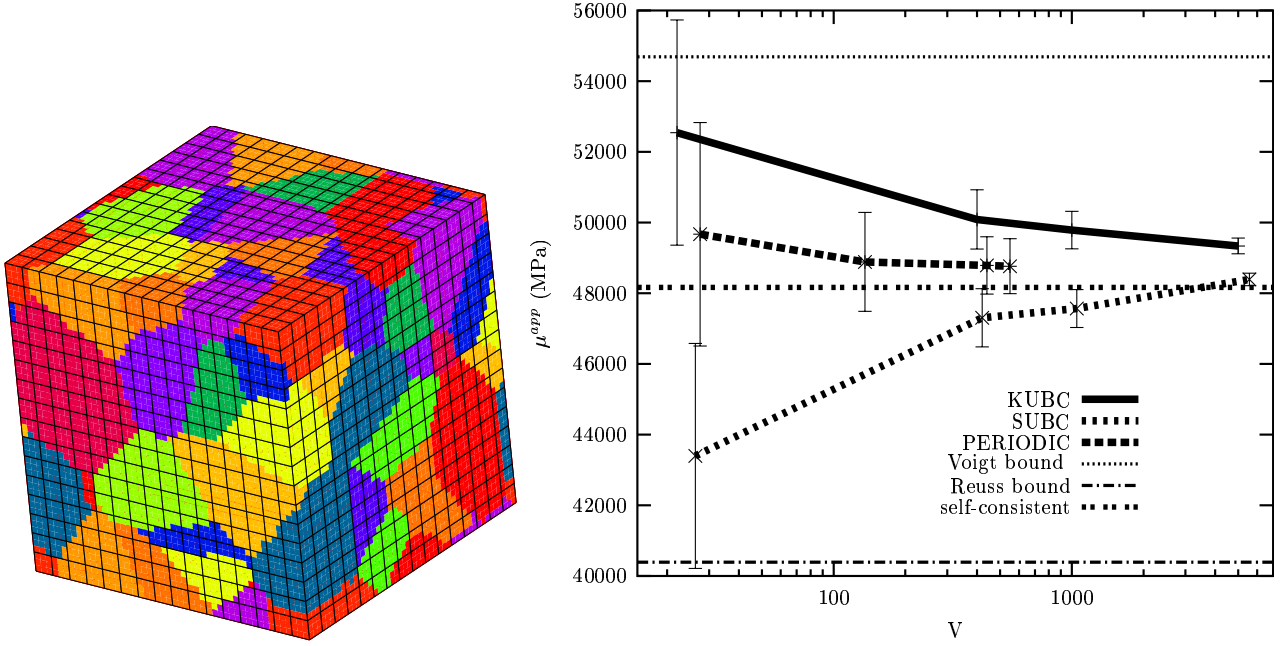


Figure 6: Apparent shear modulus for isotropic bulk polycrystalline copper as a function of volume size, after (El Houdaigui et al., 2007a)

at 300 K. The effective behaviour of such a polycrystal is isotropic. It is characterized by its bulk modulus which is identical to that of the cubic single crystal, and by its shear modulus which is estimated here by means of finite element simulations. The statistical approach yields the results of Figure 6 which shows a rapid convergence of the apparent shear modulus, when using periodic boundary conditions, towards a value close to the self-consistent estimate. It turns out that the effective shear modulus is estimated with a relative precision of 1% by means of 20 realizations of the polycrystals made of 200 grains in average.

The question of RVE size can be extended to thin polycrystalline films which possess only a few grains within the thickness, as illustrated in Figure 7. Thin films are produced from Voronoi tessellation by random slices of the bulk volumes with fixed thickness. The upper and lower surfaces are free of forces whereas periodic boundary conditions are applied in the film plane. This corresponds to a mixed type of boundary conditions. Again, isotropic distributions of lattice orientation is considered. For the statistical analysis the in-plane dimensions of the plate are increased for a constant grain size whereas the film thickness is unchanged. Several questions arise. First, how many grains within the thickness are needed to retrieve the elastic properties of the bulk materials? This questions can be answered using the statistical approach and finite element simulations carried out by (El Houdaigui et al., 2007b) show that 3 to 5 grains are sufficient in the thickness to recover the bulk properties, depending on the wanted precision.

A second question is: how much does the in-plane C_{66} and out-of-plane C_{44} shear moduli differ for a thin film with one grain within the thickness in average? It is found that the effective properties of the film differ from that of bulk copper, as shown in Figure 7. The in-plane shear modulus is found to be closer to the bulk one than the out-of-plane effective shear modulus. These results have implication for the properties of metallic films and coatings used in industry.

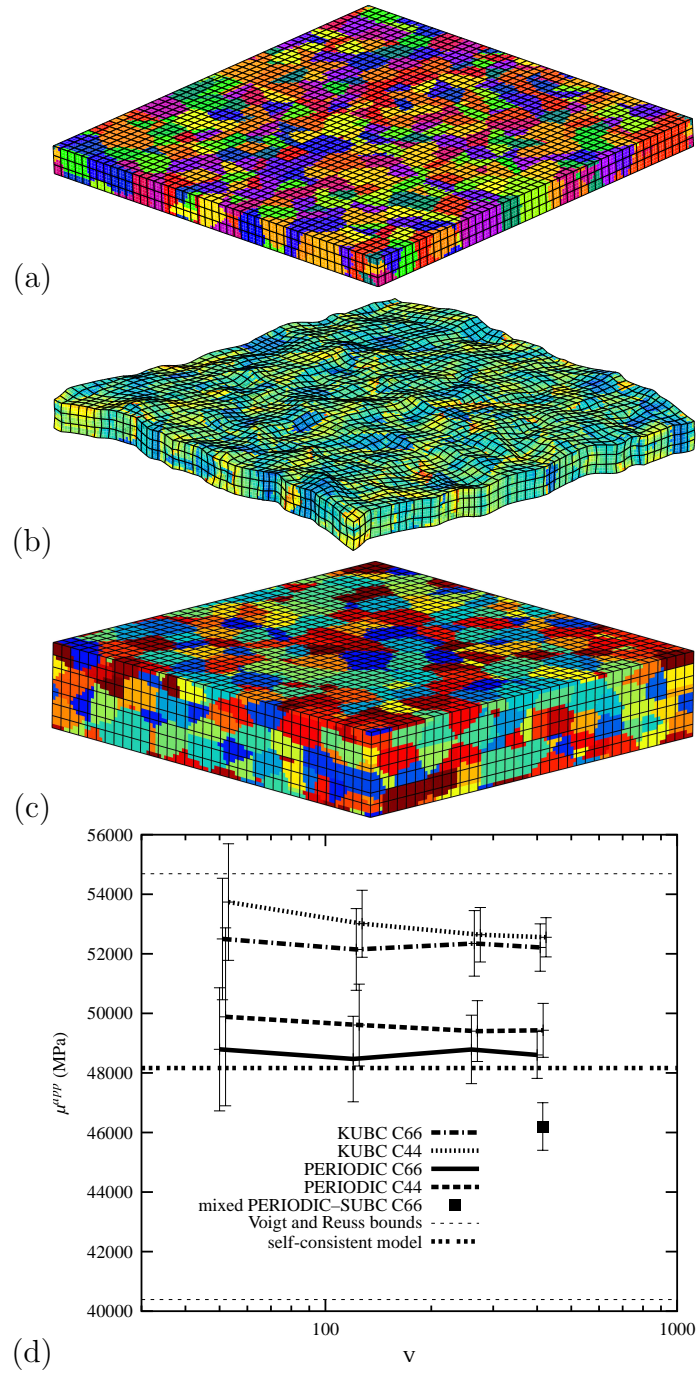


Figure 7: Apparent shear modulus of polycrystalline thin films: (a) example of film with one grain within the thickness and (b) its deformed state after in-plane shear with stress concentration contour (centre); (c) example of a thin film morphology with 3 grains within the thickness, (d) apparent shear moduli of the one-grain thick film depending on system size and type of boundary conditions

4.1.7. Granular media studied by microtomography

The two examples introduced now are based on 3D FFT computation of fields in granular materials from images obtained by microtomography: the first one concerns a propellant material made of spheroidal grains embedded in a polymer matrix (Willot et al., 2013). The second material is a mortar (Escoda et al., 2011). After a morphological segmentation of images, FFT computations provide thermal and elastic fields. In addition to the estimation of the apparent properties and of their statistical RVE, a morphological analysis of the fields provides instructive information on local field concentrations, not detailed here.

Granular material. A $(926 \times 926 \times 463)$ image is extracted from a microtomographic image obtained on a cylinder of a propellant material. Two segmentations provide either disconnected grains, or a connected microstructure with slightly overlapping grains. The thermal response of the image is obtained by the FFT method, with the following conductivities, obtained from experimental measurements: $\lambda_1 = 0.15 J/mKs$ for the matrix and $\lambda_2 = 0.609 J/mKs$ for grains. A macroscopic temperature gradient with averages $\langle \partial_i T \rangle = \Delta T_0 \delta_{ij}$ is applied, with periodic BC. The elastic response is computed for isotropic elastic moduli of components with two sets of parameters: for the matrix, i) $G = 1/2$, $K = 1/3$; ii) $G = 1/2$, $K = 2/3$; elastic properties of grains are the same up to a factor 2. Two macroscopic conditions are imposed: hydrostatic strain loading and shear strain loading. Full field calculation is made on the two segmentations. The apparent conductivity is isotropic with, for the connected microstructure, $\lambda^{app} \simeq 0.387$, close to the lower Hashin-Shtrikman bound HS^- (0.368) (Willis, 1982), as expected for a granular medium, see chapter 18 in (Jeulin, 2021). The integral range of the heat flux is $A_3 = 13^3$ and its point variance $D_q^2 = 0.23$. The statistical relative precision is very good, due to the low contrast: $\epsilon_{rela} = 0.4\%$. The apparent elastic properties in case i) are $G^{app} = 0.6534$, and $K^{app} = 4455$, very close to HS^- . With this very low contrast a recourse to numerical homogenization seems superfluous. However, the examination of full fields with a relatively high space resolution gives an interesting insight into the local response of the medium: local hot spots of the heat flux appear in the matrix at the interface between close grains, on parts of grain boundaries orthogonal to the macroscopic temperature gradient. Similar local maxima are seen for the component of the temperature gradient parallel to the macroscopic gradient. These hotspots slightly increase the point variance of the fields, and might alter the sustainability of this material if submitted to a thermal shock during its storage.

Mortar microstructure. A 3D gray scale image ($1000 \times 1200 \times 1000$ voxels, $25\mu m$ per voxel) of a mortar sample is obtained by microtomography (Escoda et al., 2011). Three components are present: voids, fine aggregates, and the surrounding matrix cement paste. In the final segmented image by a morphological procedure detailed in (Escoda et al., 2011) and chapter 19 in (Jeulin, 2021), a 3-phase microstructure is obtained with aggregates ($V_V = 0.334$), cement matrix ($V_V = 0.64$) and voids ($V_V = 0.0235$). Elastic fields are computed by iterations of FFT for two types of loading conditions and with periodic BC, as before: hydrostatic strain loading, and shear strain loading. To deal with the presence of voids, the augmented Lagrangian algorithm (Michel et al., 2000) is used on images with 500^3 or 735^3 voxels. The contrast is monitored by the ratio of Young's moduli of aggregates and of the matrix, $c = E(a)/E(m) = 10^{-8}$, 3, 100, 1000, 10000 with a fixed value for $E(m)$. The contrast $c = 3$ corresponds to the real medium. Other ratios enhance the contrast and allow us to anticipate the situations of damage (10^{-8}) or of creep ($c \geq 100$). When $E(m) = 20MPa$ and $E(a) = 60MPa$, the apparent Young's modulus is $E^{app} = 27.7GPa$, consistent with the experimental value ($26.4GPa$), which is expected for a low contrast ($c = 3$).

Concerning the RVE for elastic fields, $\epsilon_{rela} = 5\%$ is reached at low contrasts ($c \leq 100$) for volumes of the order of $V_0 = 500^3$ voxels. In the rigid case, the precision of the results remains between 5.4% and 11.4% for the given volumes. The morphological RVE for $\epsilon_{rela} = 5\%$ is much larger than the specimen size for pore volume fraction (1676^3), due to its low value and to an heterogeneous distribution of voids in the available image.

In a complementary study (Escoda et al., 2016), the same approach is applied to virtual concrete materials generated by multiscale simulation of three families of Poisson polyhedra to reproduce the size distribution of aggregates. Grains are randomly located by a sequential algorithm, without overlaps. Elastic fields are computed by FFT on large 3D simulations (1600^3 with $0.09mm/voxel$) with three scales of polyhedra. For comparison, a separation of scales is assumed, to introduce in a smaller size computation (in terms of voxels: 1024^3 with $0.24mm/voxel$) a two components medium containing large gravels and a composite matrix made of cement and of smaller gravels with elastic properties estimated from a former homogenization. This simplified approach lowers the computational cost. The predicted moduli are very close: $K^{app}/K_m = 9.0$ for 3 scales, 10.5 for scale separation; $G^{app}/G_m = 10.3$ for 3 scales, 11.5 for scale separation. The relative precision of estimates is very high, since the RVE for $\epsilon_{rela} = 5\%$ are in the range 266^3 - 308^3 , depending on the moduli and on the type of calculation.

4.1.8. Particulate random composites

Two-component random media made of non overlapping particles with a single volume v (spheres or ellipsoids) are simulated in (El Moumen et al., 2015) for low volume fractions ($V_V = 0.13$ and 0.23). The elastic properties K^{app} and G^{app} are estimated by finite elements with periodic boundary conditions. The integral range deduced from equation (24) with a point variance estimated by equation (27), and fitted from simulated moduli, is compared to a proposed expression of the integral range (V_V/N_V), N_V being the number of particles contained in the volume V . The integral range in that case does not depend on the shape of particles. The two estimates of A_3 are in good agreement. We have to point out that two implicit approximations are used by the authors: first, for a vanishing volume fraction of non overlapping particles with a large separation, the integral range of the mosaic model given by equation (31) is recovered, so that in the present case $A_3 \simeq v = V_V/N_V$. A lower value of A_3 is expected for higher volume fractions, since for a hard-core process generated by the particles the set covariance $\overline{C}(h)$ presents negative correlations for some specific distances h . The second approximation concerns the use of equation (27) in the presence of a low contrast of elastic moduli.

In the remaining part of the paper, the authors look at the change of the volume of the RVE with particulate volume fraction. Apparently using the expression V_V/N_V for A_3 and ignoring the variations of N_V , inconsistent with the change of V_V , they predict a maximum of the volume of the RVE for $V_V = \frac{2}{3}$, which is incorrect: using the correct approximation of the integral range $A_3 \simeq v = v$ and equation (27), a maximum of the volume of the RVE is expected for $V_V = \frac{1}{2}$.

It would be interesting to extend this work to a population of particles with different volumes. In that case, equation (31) should be used for a first approximation of A_3 .

As reminded in subsection 4.1.7, for a medium of this type with reinforcing non overlapping particles, a good estimate of the effective properties is provided by the lower Hashin-Shtrikman bound HS^- . Therefore, the point variance deduced from this model (see (Bornert and Suquet, 2001) p. 71, (Jeulin, 2021), p. 688 and p. 690) would be more appropriate than equation (27)

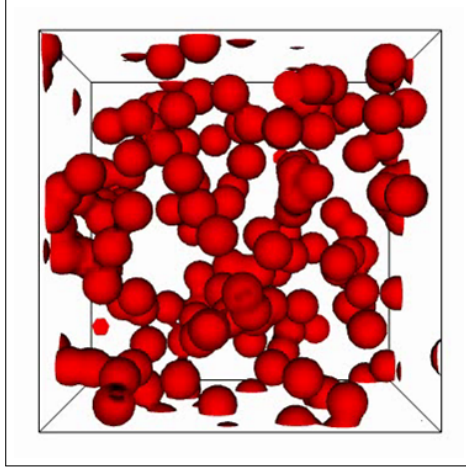


Figure 8: 3D Simulation of a Boolean model of spheres

used in this paper.

4.1.9. Boolean models by FFT

The effective bulk modulus of the Boolean model of spheres (with diameter 18 voxels), illustrated by Figure 8, is estimated by iterations of FFT from 10 realizations with size 256^3 covering the full range of volume fractions (Willet and Jeulin, 2009). Two extreme situations are explored: the porous case (for spheres with zero moduli) and the rigid case (in fact for a very high contrast, with $K_1 = G_1 = 10^3$ in spheres and $K_2 = G_2 = 1$ in the matrix). Elastic fields computation is made by means of the augmented Lagrangian version of the FFT algorithm, well adapted to infinite contrast (Michel et al., 2000), applying a macroscopic deformation equivalent to a hydrostatic loading ($\langle e_m \rangle = 1$). The effective bulk moduli K^* is subject to percolation effects: K^* vanishes for a 0.95 pore volume fraction (the solid phase being then disconnected) and starts to increase in the rigid case for a sphere volume fraction close to 0.29 for which spheres percolate.

Integral ranges are estimated from the statistics of field averages at different scales, and are plotted in Figure 9 as functions of the sphere volume fraction, after normalization for a sphere with unit diameter. The integral range of the microstructure, obtained by direct calculation from the theoretical expression of the covariance of the Boolean model of spheres, is lower than the integral range of the mean stress component σ_m , except for very high pore volume fraction, or for sphere volume fraction lower than the percolation threshold in the rigid case.

4.1.10. Multiscale media by FFT

Two-scale and three scale random media generated by Cox Boolean models can show a lowering of the percolation threshold, as compared to the Boolean model (subsection 4.1.9). The impact of this change of morphology on the effective properties of composites is studied by means of numerical simulations and iterative computations of fields by FFT for a high contrast of properties of various Cox Boolean models (Willet and Jeulin, 2011). The two-scale model is a three parameters model, obtained by keeping Poisson germs falling in a first Boolean model of spheres (with large radius R_1), the two scales having the same volume fraction $V_V^{1/2}$. Small spheres of the second scale and final model have a radius $R_2 \ll R_1$. An example of simulation of a two-scale 2D Cox Boolean model is given in Figure 10. The three scale model is similar,

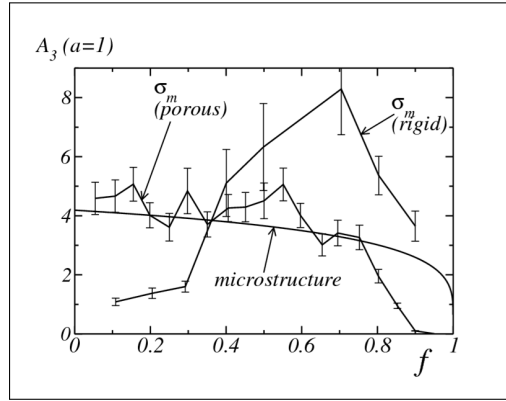


Figure 9: Integral range of σ_m , for porous and rigid Boolean models of spheres as a function of sphere volume fraction f . A_3 is normalized for a sphere of diameter 1 (Willot and Jeulin, 2009)

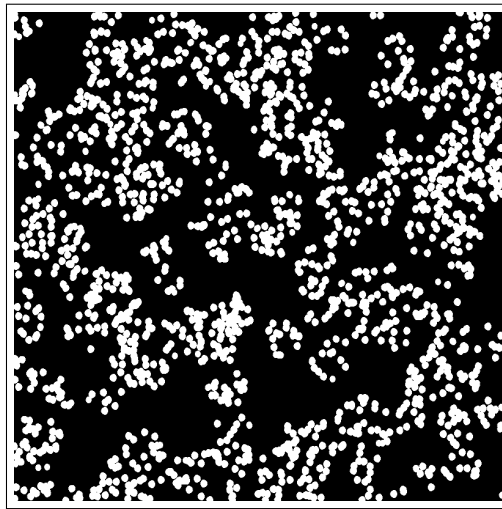


Figure 10: Example of simulation (800×800) of a 2D Cox Boolean model of discs with radius 5 pixels with centres inside a Boolean model of discs with radius 32 pixels

with an additional intermediary scale and a final radius $R_3 \ll R_2 \ll R_1$, each scale having the volume fraction $V_V^{1/3}$. For each type of microstructure, four realizations are generated in domains B with 512^3 or 750^3 voxels.

The statistical relative precision of estimated apparent properties is in the range 1 – 5% for almost all simulations. The effective conductivity, estimated for a 10^4 contrast, is much more sensitive to percolation effects than the elastic properties.

Since the largest RVE sizes for the one-scale model correspond to rigidly-reinforced media with $V_v \approx 0.7$ (cf. Figure 9), the variances $D_Z^2(V)$ and D_Z^2 , with $Z = \sigma_m$ (1/3 of the trace of the stress tensor), are estimated for the two-scales Cox Boolean model when $V_{v1} = V_{v2} = 0.7$ for a contrast higher than 10000 of the bulk and shear moduli, and a scale ratio equal to 10. It is found that the integral range of the two-scales medium is increased by a factor close to 5.8 times, whereas the point variance increases by a factor 32. A 10% precision (i.e. $\epsilon_{rela} = 0.1$) is achieved when $V \approx 550^3$, which corresponds to an increase of the RVE by a factor $5.8 \times 32 = 5.7^3$. The dramatic increase of the point variance in the case of the two-scale random medium underlies very large local stresses, that could induce more damage in the matrix if it

contains defect, as compared to the one scale model for the same volume fraction. Larger RVE, combined to the difficulty of observation of multiscale microstructures in single images, make the experimental study of such materials and their simulation much more challenging than their theoretical approach, for which some approximations of physical properties are obtained based on the assumption of a large separation of scales.

4.2. Elastic and viscoelastic properties of nanocomposites

The prediction of properties of rubber reinforced by carbon black fillers (CB) is of major importance to improve the quality of tyres in industry. Elastic and viscoelastic properties of rubber reinforced by CB were estimated from simulations of the microstructure. In (Jean et al., 2011a) and chapter 6 of (Jeulin, 2021), a three steps Cox Boolean model is identified from TEM micrographs, to locate CB nanoparticles inside spheroidal aggregates and outside of exclusion zones. In (Figliuzzi et al., 2016) a variant of this model replaces the exclusion zones made of a Boolean model of spheres by a Johnson Mehl mosaic, and carbon black aggregates are located in a second Boolean model of spheres.

4.2.1. Elastic properties

The prediction of elastic properties of carbon black rubber composites is made by FE and by FFT in (Jean et al., 2011b). For FE calculation, priority is given to generate a FE mesh that follows the microstructure interfaces, according to the conforming meshing technique. FFT calculations are made with the augmented Lagrangian algorithm (Michel et al., 2000), on 3D images with different volumes: 200^3 , 350^3 , and 500^3 for a voxel size of $3.2nm$. It is applied to two versions of simulations, images used as input for FE, which are not periodic, and a slightly modified version to get periodic images.

The shear modulus estimated by FE from SUBC and KUBC converges for the largest volumes (from $(800nm)^3$). The elastic response computed by FFT for large volumes, is in good agreement with FE computations. The obtained shear modulus is $G^{app} = 2.4MPa$, close to the lower Hashin Shtrikman bound, while the measured one is $G^{ex} = 1.81MPa$. This overestimation may be due to the presence of a layer of elastomer with weaker properties around carbon black particles, or to the morphological parameters identification from TEM images.

Integral ranges of the field estimated by application of equation (24) are $A_3^{SUBC} = 3 \times 10^7 nm^3$ and $A_3^{PBC} = 1.06 \times 10^7 nm^3$, insuring a correct statistical estimation of G^{app} for the largest simulated volumes (cube with edge equal to $1500nm$ and volume $V = 337.5 \times 10^7 nm^3$).

4.2.2. Prediction of viscoelastic properties by FFT

To predict the viscoelastic properties from the microstructure of carbon black reinforced rubber studied from TEM images (Figliuzzi et al., 2016), simulations of two-scales Cox Boolean models are generated by implantation of random spheres in a Johnson-Mehl mosaic. Viscoelastic moduli are estimated from FFT computations on simulated images. Two components are considered: the filler with an elastic behaviour, and the matrix with a viscoelastic behaviour obtained from complex elastic moduli, viscous effect being accounted for by their imaginary part. The same approach as for elastostatics is followed, using now complex properties and fields. The discrete scheme of (Willet and Pellegrini, 2008) is used to compute the fields by iterations of FFT. The local properties are set to 78 400 and 30 000 MPa for the bulk and shear moduli of the filler. For the polymer, a viscoelastic law with Prony series given in (Lairinandrasana et al., 2012) is used for 23 frequencies. Domains with volume

$(0.8\mu m)^3$ digitized on 400^3 voxels are simulated. Hydrostatic strain loading and shear strain loading are applied.

The relative precision of the estimated moduli is calculated from the variance of the fields at different scales. At a frequency $\omega = 117Hz$, the relative precision for the real part and the imaginary part of K^{app} is equal to 0.2% and to 0.3%. For the real part and the imaginary parts of G^{app} , it is equal to 17% and 3.8% respectively.

This study was followed by intensive simulations on 4000 realizations of the model with different input parameters on 512^3 images, to cover a wide range of apparent properties (Koishi et al., 2017). The simulations made on the largest supercomputer TSUBAME in Tokyo University provided a large set of results to a data mining procedure, to apply a multi-objective optimization process in order to design new filled rubber nanostructures with improved usage properties.

4.3. Optical properties of nanocomposites

Several studies are oriented towards the estimation of maps of the electrostatic fields $E(x)$ and $D(x)$ for validation of the approach, and to get indications on fields fluctuations and on the statistical RVE (Moreaud, 2006; Jeulin and Moreaud, 2008). In the context of a quasistatic approximation valid for light wavelengths λ larger than the scale of the nanostructure, the effective dielectric permittivity $\epsilon^*(\lambda)$ is then used to predict the change of optical properties of a random medium with the wavelength λ . This is illustrated for two examples of applications to paints.

4.3.1. 2D Dielectric random media

Simulations of 2D models of autodual random sets (where the morphological properties of the two components are identical, and therefore with surface fraction 0.5) provide interesting examples of Digital Materials for testing numerical homogenization tools. Indeed, the exact effective permittivity ϵ^* of 2D autodual random sets and the fields variance are known, as recalled in (Jeulin, 2021), chapter 18. For an autodual random set in \mathbb{R}^2 , the effective permittivity is given by the geometric average (Matheron, 1967):

$$\epsilon^* = \sqrt{\epsilon_1 \epsilon_2} \quad (33)$$

The theoretical point variance of the i component of the dielectric displacement $D(x)$, obtained from an applied average electric field E , is given by ((Jeulin, 2021), p. 688):

$$E \{ (D_i(x) - \epsilon^* E_i)^2 \} = \frac{1}{2} E_i^2 \sqrt{\epsilon_1 \epsilon_2} (\sqrt{\epsilon_1} - \sqrt{\epsilon_2})^2 \quad (34)$$

For comparison, three models of autodual random sets (RS) are simulated, each realization being periodic. The integral range A_2 of their set covariance is estimated as usually, from the scaling law given by equation (24) applied to the variance of local area fractions. The simulated models are:

- a symmetric colour Dead Leaves of discs (see (Jeulin, 2021), chapter 11) (Figure 11) with a 10 pixels diameter (theoretical $A_2 = 54.234$ pixels², experimental $A_2 = 54.239$ pixels²)
- two excursion sets of Gaussian RF: one obtained asymptotically from Dilution RF ((Jeulin, 2021), chapter 15) with discs with a 10 pixels diameter (Dil) ($A_2 = 4.64$ pixels²), and one with a Gaussian covariance ((Jeulin, 2021), chapter 4) ($A_2 = 5.23$ pixels²).

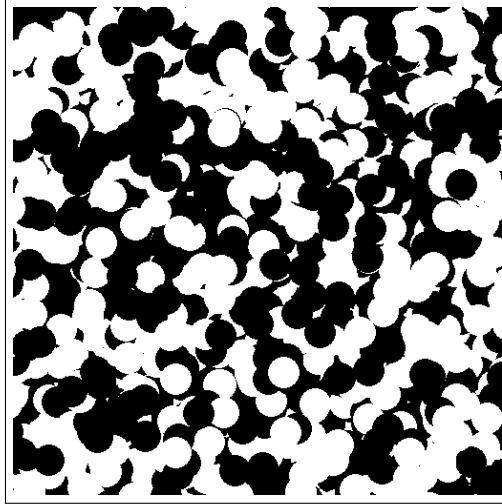


Figure 11: Simulation of an autodal RS: Symmetric Dead Leaves of discs (non periodic 512×512 image)

These models show very different morphologies, but own the same effective properties given by equation (33). The dielectric displacement field $D(x)$ is computed from simulations by FFT, applying an average electric field E_0 in the horizontal direction Ox , and using the Eyre-Milton algorithm (Eyre and Milton, 1999). Sizes of images are in the range $32^2 - 2048^2$. For the white phase $\epsilon_1 = 1$. The dielectric contrast c is monitored through $\epsilon_2 = 2, 10, 100, 1000, 10000$.

The values of the apparent dielectric permittivity ϵ^* and the point variance of D_x , for $E_x = 1$, are in excellent agreement with the theoretical values given by equation (33) ($\sqrt{\epsilon_1 \epsilon_2}$) and by equation (34). It is important to notice that the variance of $\epsilon(x)$, obtained from equation (27) ($0.25(\epsilon_2 - \epsilon_1)^2$), is much larger than the point variance of D_x . Its use to estimate the integral range would under-estimate it by a factor equal to 2.74 for $c = 10$ and to 509 for $c = 10^4$! It is therefore wise to use the correct point variance to get a correct estimation of the scale carried by a physical field. Otherwise some erroneous conclusions can be drawn, like an apparent decrease of the integral range of the field with c (Jeulin, 2005). However, sampling calculations to evaluate the RVE size, as shown in previous studies, are correct when using as input the experimental variance $D_z^2(V)$.

The integral range of the component D_x is always larger than the corresponding value A_2 for the area fraction and increases with the contrast c . The 5% relative precision RVE for a single realization depends on the random model: it is in the range $64^2 - 256^2$ when $c = 10$ and from 256^2 to 1024^2 when $c = 1000$.

4.3.2. 3D Boolean model of spheres

Boolean models of spheres (with diameter 10 voxels) are simulated for three nominal volume fractions p (0.2, 0.3 and 0.5) (Moreaud, 2006), (Jeulin and Moreaud, 2008). The matrix has a permittivity $\epsilon_1 = 1$ and spheres a larger permittivity with increasing contrast $\epsilon_2 = 10, 100, 1000$. Fields $D(x)$ are estimated by iterations of FFT with application of an horizontal field E_x , with $E_y = E_z = 0$. The effective permittivity, obtained from 10 realizations on 256^3 periodic images, is obtained as a function of p and of the contrast c . Results are close to the lower third order Beran bound (Beran, 1965) for $c < 100$ and $p < 0.3$, and to the upper bound for $p = 0.5$. Overall, bounds and the self-consistent model provide a poor prediction for this model.

The RVE V_{RVE} to estimate ϵ^* with a relative precision better than 5% is given by $V_{RVE} = 32^3$, 64^3 , 128^3 for a contrast $c = 10$, 100 , 1000 and $p = 0.3$. Point variance and integral ranges are estimated from 256^3 simulations. The microstructure integral range A_3 , theoretically calculated from the covariance, is underestimated by 10-15% in simulations. Except for a low contrast and a low volume fraction, the integral range of D_x is larger than A_3 and strongly increases with contrast, like the point variance.

4.3.3. Optical properties of paints

TiO₂ paint. In (Azzimonti et al., 2013), the prediction of optical properties of simulated deposit models for paints is investigated. The coating is a mixture of various components with different permittivity. The optical properties (and their change with the light wavelength λ) of the layer are governed by the effective permittivity of the mixture, since the optical index is given by $n = (\epsilon^*)^{0.5}$. Paint coatings are simulated by a random deposition process of nanoparticles with different shapes: spheres, or rhombus-shaped inclusions. The typical size of the nanoparticles being much smaller than the light wavelengths, electrostatics can be used to estimate ϵ^* . This is made from electrostatic fields computed by iterations of FFT on simulated paint layers (in 1200^3 voxels volumes), using the complex dielectric function $\epsilon(\lambda)$ of the TiO₂ pigment and of the matrix glass. Since the deposit shows transverse isotropy, this property appears in the permittivity tensor with the following diagonal components: $\epsilon_{xx}^* = \epsilon_{yy}^*$ and ϵ_{zz}^* . Hot spots (similar to the thermal case in subsection 4.1.7) are generated on the field maps, around corners of very close rhombus nanoparticles, or between two nearly-touching spherical inclusions, when the zone of contact is orthogonal to the applied macroscopic field E . For these simulations, this effect is stronger for the imaginary part of the displacement field, which generates colour on the macroscopic scale.

The size of the RVE of $D(x)$ is much larger than the pigment size, in particular for its imaginary part as a result of hot spots. The relative precision of the estimation of the average real part of D ($\text{Re}(D)$) is 0.82%. It is not so good, but acceptable for the average of its imaginary part $\text{Im}(D)$ (8.84%). A 1% relative precision would require the simulation of a volume made of 204^3 voxels for the volume fraction V_V , 1050^3 for $\text{Re}(D_x)$ and 5130^3 for $\text{Im}(D_x)$.

Hematite coating. In a second study, a calibrated paint with an epoxy resin containing a dispersion of hematite nanocubes with 0.1 volume fraction is modelled by a two-scale random set after identification of its parameters from quantitative SEM image analysis on $30\mu\text{m} \times 30\mu\text{m}$ images (Couka et al., 2015b). On the scale of a few micrometers, aggregates of hematite nanoparticles (similar to dice with round edges and corners, and with diagonal close to 300nm) are organized along thin curved channels. A two-scale random model was developed to simulate the dispersion of nanoparticles: cubic nanoparticles with uniform orientations are located according to a random sequential addition RSA hard core model of spheres outside of exclusion zones, almost free from hematite particles. Nanoparticles are packed by translation until intersection. For real SEM images and for simulations, the 2D integral range of the area fraction obtained on sections is $A_2 = 3.52 \times 10^{-2} \mu\text{m}^2$, so that the area fraction of a single 2D image is obtained with a 11.7% relative precision.

Ellipsometry measurements of the complex refractive index as a function of the light wavelength (in the range $381\text{nm} - 881\text{nm}$) are used to estimate the anisotropic permittivity of hematite particles, the permittivity of the resin and of the coating (Couka et al., 2015a). The apparent permittivity is estimated from FFT full field computations of the complex dielectric displacement D on a realization of the 3D random model containing 99886 nanoparticles

digitized on a grid of 500^3 voxels with a resolution of $31nm/voxel$, so that each nanoparticles is digitized as a cube of about 5^3 voxels. The visible spectrum is digitized in 24 equispaced values for $\lambda = 381 - 781nm$.

For illustration, the relative precision obtained from statistical RVE computation by means of the integral range derived from equation (24) fitted from subvolumes of a large simulation is given for three wavelengths and a single 3D image in the Table below. When $\lambda = 441nm$, a volume $V = 4285^3$ voxels corresponding to $132.8\mu m^3$ is required to reach a precision better than 0.1% for $\text{Im}(\varepsilon^*)$. The largest RVE corresponds to the lowest wavelength ($\lambda = 441nm$).

$\lambda(nm)$	441	621	800
relative precision $\text{Re}(\varepsilon^*)$	1.29%	1.27%	0.92%
relative precision $\text{Im}(\varepsilon^*)$	2.51%	0.21%	0.36%

The predicted apparent permittivity from FFT computations on simulated microstructures is very close to the measurements on a sample of hematite coating, except for the imaginary part on shortest wavelengths, for which the quasi-static approximation reaches its limits.

4.4. Fluid flow and permeability

The emergence of Darcy's law on a macroscopic level is a direct outcome of the linear character of the Stokes equation (3) obtained from Navier-Stokes equations by linearisation while neglecting inertial effects, for a fluid with viscosity μ (Matheron, 1967), combined to the continuity equation for incompressible fluids

$$\partial_i u_i = 0 \quad (35)$$

and with the following boundary condition (no slip) applied on pore boundary

$$\partial A : u_i(x) = 0 \text{ for } x \in \partial A$$

On a macroscopic scale, the fluid flow satisfies Darcy's law relating the fluid flux Q^i to the pressure gradient $\partial_i P$:

$$\langle u_i \rangle = Q^i = -\frac{1}{\mu} K^{ij} \partial_j P$$

The permeability K has the dimension of a surface (length^2), and is usually expressed in cm^2 . The BC acting on the pore boundary with a complex geometry differ from the conditions operating in electrostatics, so that generally the permeability K cannot be deduced in a simple way from the permittivity or the resistivity of the porous medium (Matheron, 1967).

The Darcy permeability of random porous media with a full range of pore volume fractions is studied by solving the Stokes equations by FFT on periodic simulations of Boolean models of spheres (Abdallah et al., 2015) and of cylinders (Willot et al., 2016). A numerical method of resolution was developed by A. Wiegmann in (Wiegmann, 2007). It relies on the resolution of four Poisson equations (one for pressure p and one for each component of the velocity u_i), the inversion of the Laplacian being obtained by FFT. The no-slip condition is constrained by forces introduced along ∂A . In (Abdallah et al., 2015) FFT solutions are obtained for a Boolean model of spheres with diameter $d = 15$ voxels generating two porous media: solid phase is the union of spheres (case A, with permeability k_A), or alternatively pores are the union of spheres (case B, with permeability k_B). Simulations in cubic volumes 100^3 , 256^3 and 512^3 are generated to cover the full range of pore volume fractions.

For a large range of pore volume fractions of the Boolean model of spheres and the two cases A and B, the size of the statistical RVE, calculated from the integral range and the point variance of the velocity field is much larger than the microstructural RVE or the RVE for elastic moduli or thermal conductivity. It strongly increases when reaching the percolation threshold.

In (Bignonnet, 2020) a different scheme is introduced to compute velocity fields on images by FFT. It makes use of a variational principle and trial force fields to produce an upper bound of the permeability. Therefore results obtained by this method should be compared to other calculations. It is used to estimate the permeability of the Voronoi mosaic for the full range of pore volume fractions on simulated images with size 512^3 . The integral range of the velocity is much larger than the integral range of volume fraction. Again the RVE size shows similar variations with p as obtained for the Boolean model of spheres in (Abdallah et al., 2015), and is the largest close to the percolation threshold (0.1453 in the present case for site percolation).

It would be interesting to estimate the Darcy permeability of multi-scale models such as Cox Boolean models. However this task may be insurmountable, since gigantic RVE are expected (as for Poisson fibres in subsection 4.1.5).

4.5. Acoustic properties and wave propagation in fibrous media

For engineering purposes, predicting acoustic properties of random media from their microstructure is a first step to design new materials with improved properties, like a better sound attenuation. One of the challenging problems to solve concerns the fluctuations of the microstructure and of the local physical fields involved in the homogenization of the acoustic behaviour (Peyrega and Jeulin, 2013). The results outlined in this subsection concern the estimation of acoustic properties of random fibres by numerical homogenization, and the study of corresponding RVE.

On the microscopic scale, viscous and thermal dissipations of energy occur in the air saturating voids of a porous medium. To predict the acoustic behaviour of random porous media, use is made of a thermoacoustic formalism on realizations. Properties like harmonic acoustic velocity and temperature are homogenized by averaging after a numerical computation of the harmonic fields (flow velocity, fluid temperature and pressure) by Finite Elements, using the FE software Comsol Multiphysics, for frequencies in the range $0 \text{ Hz} - 4032 \text{ Hz}$. More details are given in (Peyrega and Jeulin, 2013) and ((Jeulin, 2021), chapter 19). Differently from other examples presented in this chapter, here one has to deal with the solutions of a dynamic problem of wave propagation.

Twenty realizations are generated for a model of random fibrous media of infinite parallel fibres, with cross sections made of three Boolean models of discs with radius $R_F = 42\mu m$, $100\mu m$ and $300\mu m$, and with average pore volume fraction 0.64 corresponding to real materials with wooden fibres used for acoustic attenuation. Square fields have the following edge lengths: 2.52, 6, 18mm. Acoustic fields are not homogeneous and local fluctuations appear, resulting in variations of the acoustic properties between realizations. For each radius, the average absorption coefficient is estimated from permeabilities averaged over the $n = 20$ independent periodic microstructures. Concerning the radius $42\mu m$, the prediction of the coefficient of absorption $\alpha(\omega)$ fits the experimental results, as for a simplified cell made of a single fibre building a regular medium. For larger fibres ($R_F = 100 \mu m$ and $300 \mu m$) the frequency evolutions are globally similar with almost identical amplitudes, but a frequency shift is observed between regular and random microstructures.

The size of the statistical RVE is estimated for properties from results on the dispersion. Concerning the area fraction, the integral range of sections is directly calculated from the

theoretical expression of the covariance of the 2D Boolean model of discs ($0.0049mm^2$, $0.0277mm^2$, $0.2495mm^2$), in agreement with estimations from simulations. The relative precision for the pore volume fraction on a single realization is $\epsilon_{rela} = 3.7\%$.

Harmonic acoustic velocity and temperature being complex variables, the estimation of the RVE operates on their real and imaginary parts. Detailed results are available in (Peyrega and Jeulin, 2013). Integral ranges A_2 , ϵ_{rela} and the RVE size of the four average scalar fields decrease with the frequency for $R_F = 42 \mu m$ and $R_F = 100 \mu m$. This can be explained by the frequency dependence of the thickness of the boundary layer of the interface pore-solid, involving a decrease of correlation lengths at high frequency. The relative precision of the four scalar fields is much better than 10 %. The RVE size does not change with frequency for $R_F = 300 \mu m$. Integral ranges of fields are much larger than the morphological integral ranges. Concerning the acoustic absorption $\alpha(\omega)$, its relative precision for 20 realizations is better than 5% for $R_F = 42 \mu m$ and $R_F = 100 \mu m$.

Finally, in the present case thermal properties fluctuate more and develop longer correlation lengths than velocity fields. The thermal properties are therefore the limiting factor to define a representative volume element in this application.

4.6. Nonlinear properties

4.6.1. Viscoplastic composite

The same approach was applied to a nonlinear behaviour, namely for 2D/3D viscoplastic composite materials (Madi et al., 2006), the creep following a simple power law with exponents 3.5 in the hard phase and 4 in the soft phase. Shear tests are simulated by Finite Elements under a macroscopic shear stress, and the statistical analysis is performed on the shear strain rate field. In that case it is found that for the same statistical precision, the linear elastic RVE is larger than the nonlinear RVE. The degree of generality of this result is not known. It is expected that in the case of a strong localization with a nonlinear behaviour, long range correlations of the fields might appear, and scaling laws similar to the dilated Poisson hyperplanes (with a scaling exponent close to $\frac{1}{3}$) might be recovered, so that a slow convergence towards the effective properties might be observed on numerical simulations, but this should be confirmed by further simulations.

4.6.2. Elastoplasticity of porous media

The yield surface for random porous elastoplastic materials was determined for the first time by (Fritzen et al., 2012) following a statistical approach. Previous studies performed since the early 1980s to analyse void growth and ductile fracture mechanisms, were limited to periodic unit cells containing a single void. The use of a random model is closer to the physical reality of engineering materials and allows for more general interactions between voids. The proposed Hard Core model of non-intersecting spherical voids of single size is illustrated in Figure 12. The elastoplastic matrix is assumed to obey to J_2 -plasticity in the absence of hardening. The yield stress is taken as $\sigma_0 = 100$ MPa. Periodic boundary conditions are applied controlling the applied axial deformation E_{11} , E_{22} , E_{33} of the cubic volume:

$$\begin{aligned} E_{11}(t) &= t\dot{\epsilon}_0(\alpha + \beta), \\ E_{22}(t) &= t\dot{\epsilon}_0(-\alpha + \beta), \\ E_{33}(t) &= t\dot{\epsilon}_0\beta, \\ \Sigma_{12}(t) &= \Sigma_{13}(t) = \Sigma_{23}(t) = 0 \end{aligned} \tag{36}$$

Time t is here a loading parameter since rate-independent plasticity is considered. It is increased until an overall limit stress state is reached for which the von Mises equivalent stress Σ_{eq} and the mean stress Σ_m (opposite to the hydrostatic pressure) are recorded for each value of the loading parameters α and β . The latter parameters explore the deviatoric and hydrostatic parts of the strain space. The values $\alpha = 0; 1/2; 1$ and $0 \leq \beta \leq 1$ are considered. The results are shown in the bottom Figure 12 and shows the yield surfaces for various values of the porosity f . They are compared to computations based on periodic unit cells (single pore model). The unit cell provides an excellent estimate of the yield locus for $f = 0.001$ but a poor prediction for high porosity $f = 0.3$. Figure 13 shows the results of the statistical approach in the form of the dependence of the asymptotic von Mises equivalent and hydrostatic stress responses as functions of the number of voids in the volume element. In the case $N = 50$, ten realizations were considered to evaluate the average which compares well with estimated for larger N values, at least for periodic boundary conditions. In contrast, uniform Dirichlet conditions only provide upper bounds.

The obtained yield functions are used by (Fritzen et al., 2012) to calibrate an effective Gurson-Tvergaard-Needleman potential with parameters taken as explicit functions of porosity f :

$$\phi = \frac{\Sigma_{eq}^2}{\sigma_F^2} + 2q_1 f \cosh\left(q_2 \frac{3\Sigma_m}{2\sigma_F}\right) - 1 - q_3 f^2 \quad (37)$$

$$\text{with } q_1(f) = \theta_0 - \theta_1 f, \quad q_2(f) = \theta_2, \quad q_3(f) = (q_1(f))^2 \quad (38)$$

The involved coefficients are identified as: $\theta_0 = 0.169$, $\theta_1 = 1$, $\theta_2 = 0.92$. This meta-model can be used for many applications within the considered porosity range.

This statistical approach was extended by (Fritzen et al., 2013) to double porosity media with separation of scales, meaning that holes are embedded in an homogenized elastoplastic matrix. The latter is endowed with a compressible plasticity model involving an elliptic yield function with respect to von Mises equivalent stress and hydrostatic stress.

Beyond limit analysis, the statistical method can be applied to the occurrence of localization phenomena and failure analysis for a Boolean model of holes, as proposed by (Cadet et al., 2021). This requires large deformation elastoplasticity formulation and detection of void coalescence phenomena. This can be performed by means of Rice's strain localization criterion applied to the effective incremental tangent behaviour of the unit cell, as done by (Cadet et al., 2022). Surface responses for the critical strain at overall localization can be predicted in that way considering various realizations of the random microstructure. In the presence of instabilities, the anisotropy bias induced by the cube shape of the volume element becomes particularly significant. In simplified approaches considering a single pore in a cube volume element, this bias is very strong. It is alleviated by consideration of a random model but still exists. That is why rotation of the loading was applied systematically by (Cadet et al., 2022) to determine the interval of fracture strain induced by spurious anisotropy effect of the volume element.

4.6.3. Elastoviscoplastic polycrystals

The plasticity of metallic polycrystals is the subject of many contributions in micromechanics of bulk crystalline solids. The question of RVE size is central in the computation of apparent nonlinear properties of polycrystalline aggregates addressed for the first time in a systematic way by (Barbe et al., 2001b, 2003). A simple model for isotropic polycrystals is the Voronoi tessellation as depicted in (Barbe et al., 2001a). It can be extended to account for more realistic and elaborate grain shape distributions, as done in (Quey et al., 2011). The Voronoi model is

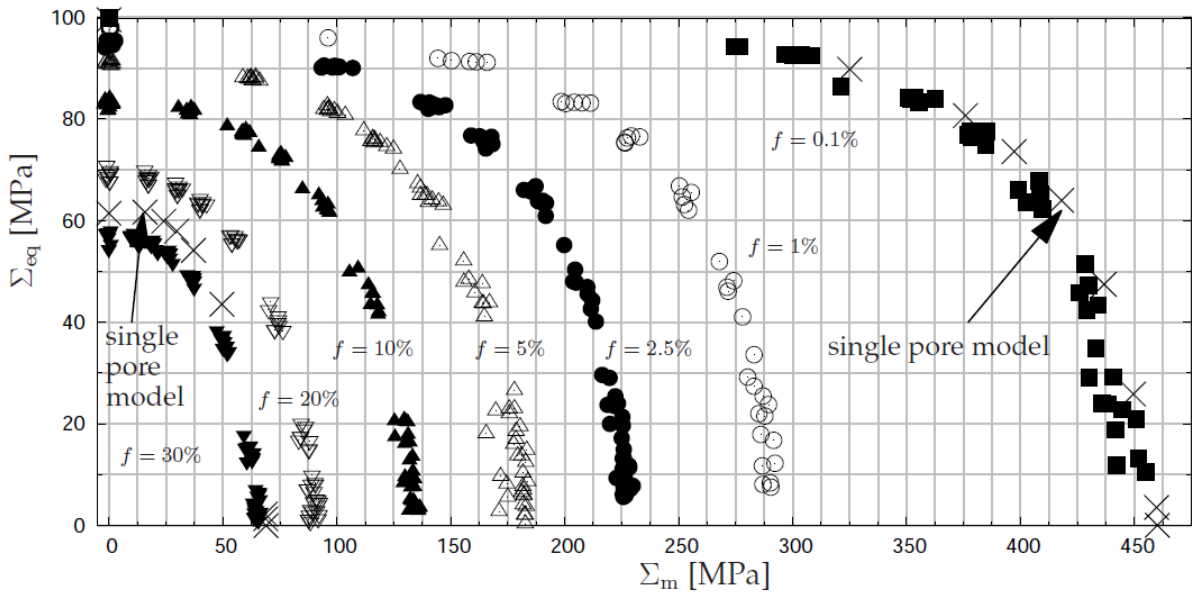
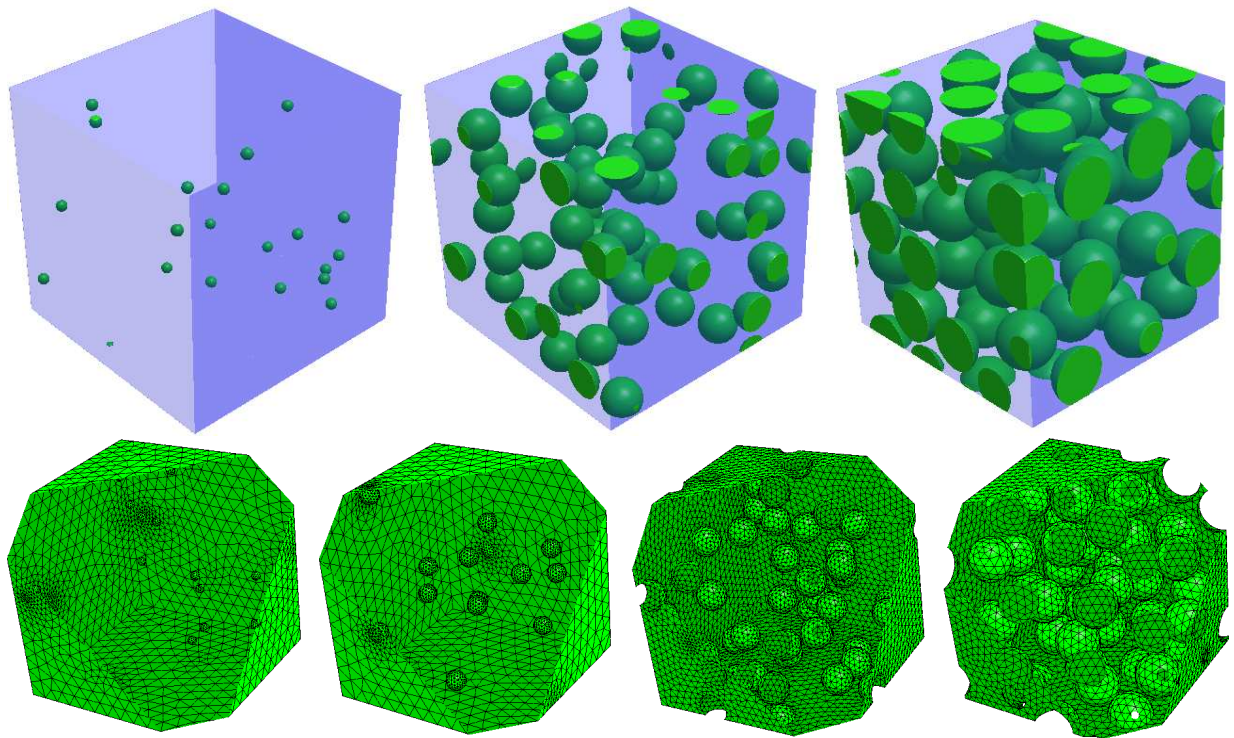


Figure 12: Hard Core model of non-intersecting spherical holes in a matrix for three volume fractions ($f = 0.001, 0.1, 0.3$ from the left to the right) and associated finite element meshes ($f = 0.001, 0.01, 0.1, 0.3$). The bottom plot shows the determined limit analysis surface for various void volume fractions, after (Fritzen et al., 2012)

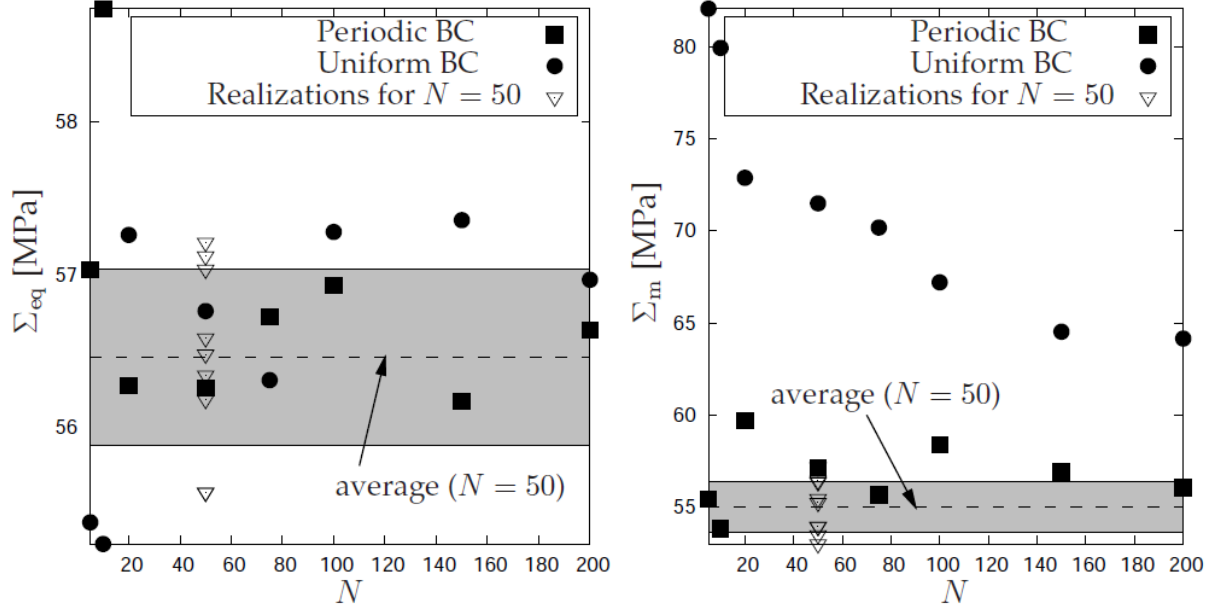


Figure 13: Comparison of the limit asymptotic von Mises equivalent stress (left) and hydrostatic stress (right) for various numbers of pores and types of boundary conditions (interval of confidence in gray), $f = 0.2, \alpha = 1, \beta = 0.25$, after (Fritzen et al., 2012)

sufficient to highlight the tremendous heterogeneity of plastic deformation in polycrystals when comparing the overall stress-strain curve to mean response of individual grains or individual material points. The description of intragranular heterogeneities goes beyond estimations by micromechanical models and is one of the greatest advances of full field polycrystal plasticity simulations. The latter are based on the appropriate choice of continuum crystal plasticity constitutive models that were developed since the early 1970s. The number of grains required in the polycrystalline aggregates to estimate with a given precision the overall response of the polycrystal is still an open question. Heuristic results are presented in the cited references but they are limited to particular loading conditions like tensile curves, cyclic loading or rolling conditions in metal forming. A systematic procedure cannot easily be defined due to the path dependent character of elastoplasticity laws. Strong non-linearities arise from the selection of activated slip systems and interaction between slip systems in the hardening functions. Large deformations and crystal lattice rotation are other sources of non-linearity of the problem.

An illustrative example is given here for polycrystalline copper films as explored by (Šiška et al., 2007a,b). Columnar grains are defined by appropriate two-dimensional Voronoi tessellation. The average in-plane grain size d is taken equal to the film thickness h . The heterogeneity of polycrystals stems from the crystal lattice orientation distribution among the grains. Thin metallic films usually possess preferential grain orientations associated with a non uniform crystallographic texture. Copper thin films discussed in (Šiška et al., 2007a,b) are characterized by the pole figure of Figure 15 (top left), with 90% of $\{111\}$ grains, 6% of $\{001\}$ grains and 4% random grains. The $\{111\}$ grains for instance, have one $\{111\}$ plane parallel to the film but the orthogonal in-plane orientation is random. In-plane periodicity is enforced and the remaining lateral surfaces are free of forces in free-standing films or one face remains flat due to the presence of a rigid substrate. Results are provided here in the latter case. The film is subjected to cyclic uniaxial in-plane tension-compression with prescribed overall strain

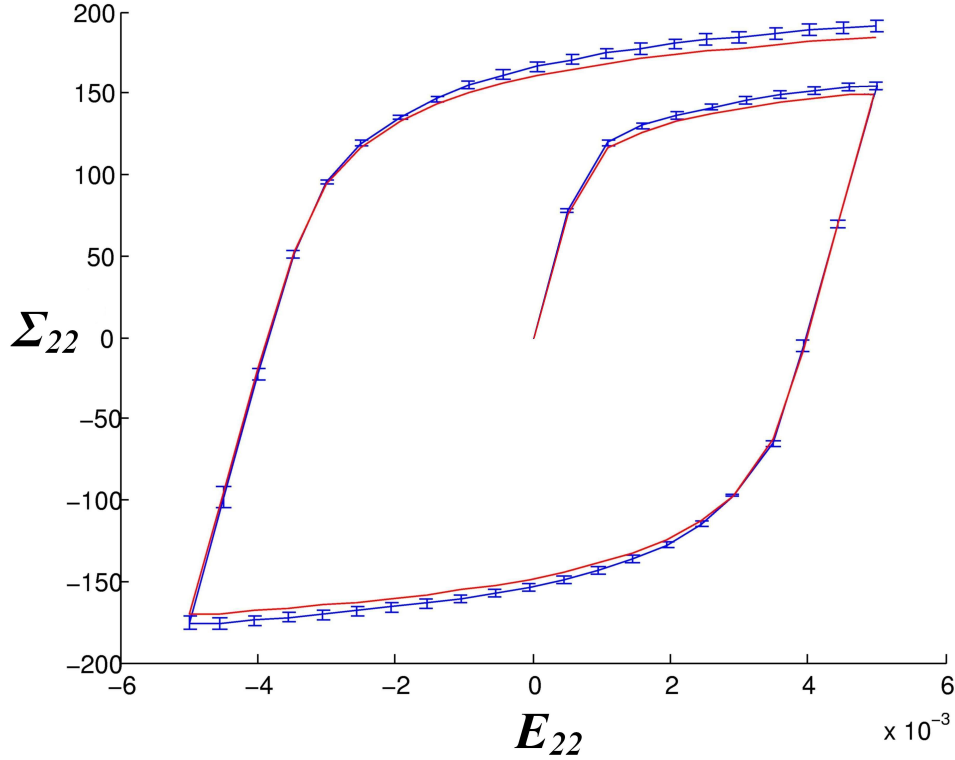


Figure 14: First cyclic overall stress-strain loop for textured polycrystalline copper thin films made of 225 grains (red curve) and ensemble average of 10 simulations with 50 grains films (blue curve) with corresponding standard deviation indicated by error bars, after (Šiška et al., 2007b)

$E_{22} = \pm 0.5\%$. The corresponding overall stress-strain response is shown in Figure 14 in the case of a 250-grain film. This estimation of the effective tension-compression behaviour of the film is compared to the ensemble average of 10 realizations of 50-grains aggregates. The cyclic loops exhibit some scatter represented by error-bars in the figure. The difference between both curves remains small indicating that the 250-grain film can be regarded as a RVE for the considered loading conditions.

Cyclic loading leads to an evolution of the stress-strain loops when increasing the number of applied cycles. Convergence of the loop is found after 100 cycles according to (Šiška et al., 2007b). The first and the stabilized loops are shown in Figure 15 for the various components of the crystallographic textures. The results are given for five realizations of 50-grains films. Almost no scatter is observed for the dominant $\{111\}$ texture component due to the sufficiently large number of grains sharing this orientation. In contrast, significant scatter is observed for the $\{100\}$ and random crystallographic texture components. It means that the obtained results may not be representative for this population of grains and number of grains larger than 50 should be considered.

The cyclic elastoplasticity behaviour of bulk FCC polycrystals was studied by (Farooq et al., 2019). The authors provide a thorough statistical analysis of the strain distribution inside the polycrystalline aggregates for complex non-symmetric stress-based or strain-based cyclic loading conditions. The results show the ability of full field crystal plasticity simulations to account for complex ratcheting and cyclic stress relaxation behaviour which is classically observed experimentally in engineering alloys like nickel-based superalloys for aeronautic applications.

The free surface behaviour of polycrystals is important not only for films but also for

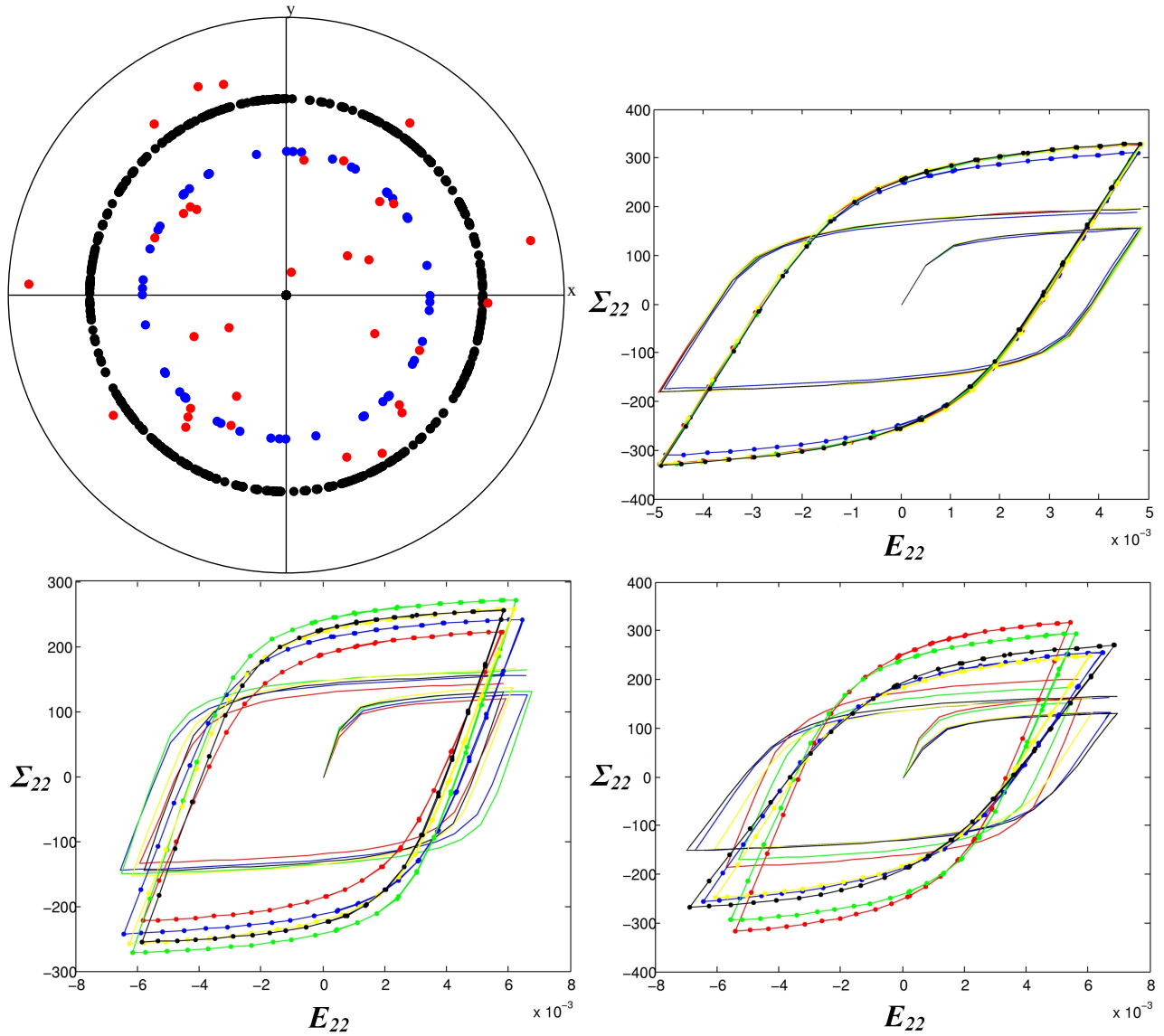


Figure 15: Crystallographic texture of the copper thin films (top left pole figure); first and stabilized cyclic loops for the average stress-strain in $\{111\}$ grains (top right), in $\{001\}$ grains (bottom left) and random grains (bottom right), after (Šiška et al., 2007b)

comparison with experimental results showing strain and lattice rotation fields at surfaces by means of standard optical or electronic microscopy methods. The major problem lies in the fact that, generally, the 3D grain morphology of underlying grain layers are not accessible to these measurements also they contribute to the surface response. Ensemble averaging methods were employed to analyse the surface behaviour of polycrystalline copper polycrystals in (Zeghadi et al., 2007b,a). For that purpose, random grain microstructures were simulated with the constraint of prescribed morphology of the intersection of the grains with the free surface and prescribed crystal orientation of surface grains. The results highlight the strong impact of 3D grain morphology on the strain and stress response at the free surface. In particular, it is demonstrated for the considered FCC material with isotropic orientation distributions that 2 to 3 grain layers are significantly affecting the surface response. This was confirmed in the case of cyclic behaviour of tantalum polycrystals by (Colas et al., 2019, 2021).

4.6.4. 2D hyperelastic Boolean random media

In (Brändel et al., 2022), the macroscopic hyperelastic parameters of 2D Boolean models with circular and rectangular grains stiffer than the matrix are estimated by homogenization, the two components following a Neo-Hooke law so that they are both hyperelastic with different coefficients. In this detailed and complete work (which is very briefly summarized here) with a full range of area fractions $A_A = 0.1 - 0.9$, finite strains in finite elasticity are applied on realizations of microstructures (512^2 images) by Finite Elements calculations with periodic BC. The Neo-Hooke strain energy Ψ is expressed as a function of the Lamé constants λ and μ by:

$$\Psi = \frac{\mu}{2}(I_1 - 3) + \frac{\lambda}{2} \ln^2 J - \mu \ln J \quad (39)$$

where $J = \det(F)$, F being the deformation gradient, and $I_1 = \text{trace}(C) = \text{trace}(F^T F)$ is the first invariant of the Cauchy-Green tensor C . In the matrix, $\lambda = 100\text{GPa}$ and $\mu = 75\text{GPa}$. For the grains the same properties are used, up to a contrast factor c in the range $2 - 100$.

A uniaxial tension test is used for identification of apparent material properties, assuming an effective Neo-Hooke strain energy Ψ^* of the same type for the composite, from the average of the components of the stress tensor over more than 200 realizations of each model of microstructure. A biaxial tension test, completed by a shear test, are used for validation of the fit obtained for λ^* and μ^* by least squares minimization of the error between the average value of $\langle \Psi \rangle$ over realizations and the theoretical expression of Ψ^* given by equation (39) with the effective parameters.

Applying the same procedure of identification on each realization, the authors obtain apparent parameters λ^{app} and μ^{app} depending on the scale of computations, for which experimental variances are computed. For each 2D Boolean model, a statistical RVE size for a single realization is computed for a 1% relative precision. In a second step, integral ranges are estimated for the apparent parameters, unfortunately using the wrong estimate of the point variance given by equation (27). As a consequence, the obtained integral ranges are strongly underestimated, and unexpectedly decrease with c in Table 4 of (Brändel et al., 2022). Instead, use should be made of the point variance and variance of the average of the stress field to deduce the integral range of this field. Nevertheless, intervals of confidence given in the paper, that are not deduced from the obtained integral ranges, are correct. It is checked that the size of simulations is large enough to get an accurate estimation of the parameters.

In the case of Boolean models of discs with a fixed radius, the size of images to reach the asymptotic estimations and the RVE size are the largest for $A_A \simeq 0.6$. We have to notice that it

corresponds to the percolation threshold of discs in 2D. When increasing the anisotropy of the primary grain (from discs to more or less elongated rectangles), the convergence of apparent properties with the size of simulations is accelerated, as a result of a better percolation of the grains. More elongated grains provide stiffer media, as already shown in elasticity, but percolation effects are amplified in the 2D case. Finally, populations of discs with a lognormal distribution of their radii are simulated. To maintain a good statistical precision and a low systematic error, larger RVE and larger number of realizations have to be used when increasing the coefficient of variation c_v of the distribution. With the given parameters, a relative precision of the order of 3% is reached when $c_v = 1$, for which the 2D medium is 20% softer than in the case of discs with a single radius.

5. Conclusion

The determination by a statistical approach of the size of the RVE to estimate effective properties by numerical simulations of Digital Materials with a given precision is now well established, after nearly two decades of development and of applications. From available data on simulations, the estimation of effective properties (linear and nonlinear elastic moduli, linear and nonlinear conductivity, flow permeability, ...) of the common Boolean model of spheres, of its multiscale versions and of other models are now well documented. Intervals of confidence of the obtained apparent properties are given as a function of the scale of computations, for a correct use of predictions from images obtained on real or on simulated microstructures. This is mandatory in order to master small scale fluctuations. The best strategy to minimize size and edge effects in numerical simulations is to operate with periodic boundary conditions, and when possible on periodic generated realizations of microstructures from some probabilistic model.

For a nonlinear constitutive behaviour, in micromechanics it is wise to estimate the macroscopic stress-strain relationships with their intervals of confidence and their own statistical RVE sizes, before estimating the parameters of the underlying constitutive equations.

Further use of this statistical approach is expected in various areas: numerical homogenization of nonlinear physical properties, damage, wave propagation, and fracture toughness as suggested in preliminary studies, see (Jeulin, 2021), chapters 20 and 21.

References

- Abdallah, B., Willot, F., Jeulin, D., 2015. Stokes flow through a Boolean model of spheres: Representative volume element. *Transport in porous media* 109, 711–726.
- Altendorf, H., Jeulin, D., 2011. Random-walk-based stochastic modeling of three-dimensional fiber systems. *Physical Review E* 83, 041804.
- Altendorf, H., Jeulin, D., Willot, F., 2014. Influence of the fiber geometry on the macroscopic elastic and thermal properties. *International journal of solids and structures* 51, 3807–3822.
- Armstrong, S., Kuusi, T., J-C, M., 2019. Quantitative stochastic homogenization and large-scale regularity. volume 352. Springer.
- Azzimonti, D., Willot, F., Jeulin, D., 2013. Optical properties of deposit models for paints: full-fields FFT computations and representative volume element. *Journal of Modern Optics* 60.

- Barbe, F., Decker, L., Jeulin, D., Cailletaud, G., 2001a. Intergranular and intragranular behavior of polycrystalline aggregates. part 1: Fe model. *International journal of plasticity* 17, 513–536.
- Barbe, F., Forest, S., Cailletaud, G., 2001b. Intergranular and intragranular behavior of polycrystalline aggregates. Part 2: Results. *International Journal of Plasticity* 17, 537–563.
- Barbe, F., Forest, S., Quilici, S., Cailletaud, G., 2003. Numerical study of crystalline plasticity: measurements of the heterogeneities due to grain boundaries under small strains. *La Revue de Métallurgie* 101, 815–823.
- Beran, M., 1965. Use of the variational approach to determine bounds for the effective permittivity in random media. *Il Nuovo Cimento (1955-1965)* 38, 771–782.
- Beran, M., McCoy, J., 1970. Mean field variations in a statistical sample of heterogeneous linearly elastic solids. *International Journal of Solids and Structures* 6, 1035–1054.
- Bignonnet, F., 2020. Efficient FFT-based upscaling of the permeability of porous media discretized on uniform grids with estimation of RVE size. *Computer Methods in Applied Mechanics and Engineering* 369, 113237.
- Bobeth, M., Diener, G., 1986. Field fluctuations in multicomponent mixtures. *Journal of the Mechanics and Physics of Solids* 34, 1–17.
- Bornert, M., Suquet, P., 2001. *Homogénéisation en mécanique des matériaux*, vol. 2. Hermès. chapter 2 Propriétés non linéaires des composites: approches par les potentiels. pp. 45–90.
- Brändel, M., Brands, D., Maike, S., Rheinbach, O., Schröder, J., Schwarz, A., Stoyan, D., 2022. Effective hyperelastic material parameters from microstructures constructed using the planar Boolean model. *Computational Mechanics* , 1295–1321.
- Buryachenko, V., 2007. *Micromechanics of heterogeneous materials*. Springer Science & Business Media.
- Buryachenko, V.A., Kreher, W.S., 1995. Internal residual stresses in heterogeneous solids—a statistical theory for particulate composites. *Journal of the Mechanics and Physics of Solids* 43, 1105–1125.
- Cadet, C., Besson, J., Flouriot, S., Forest, S., Kerfriden, P., Lacourt, L., de Rancourt, V., 2022. Strain localization analysis in materials containing randomly distributed voids: Competition between extension and shear failure modes. *Journal of the Mechanics and Physics of Solids* , 104933doi:[10.1016/j.jmps.2022.104933](https://doi.org/10.1016/j.jmps.2022.104933).
- Cadet, C., Besson, J., Flouriot, S., Forest, S., Kerfriden, P., Rancourt, V.d., 2021. Ductile fracture of materials with randomly distributed defects. *International Journal of Fracture* 230, 193–223. doi:[10.1007/s10704-021-00562-7](https://doi.org/10.1007/s10704-021-00562-7).
- Cailletaud, G., Jeulin, D., Rolland, P., 1994. Size effect on elastic properties of random composites. *Engineering computations* 11, 99–110.

- Colas, D., Finot, E., Flouriot, S., Forest, S., Mazière, M., Paris, T., 2019. Local ratcheting phenomena in the cyclic behavior of polycrystalline tantalum. *JOM Journal of the Minerals, Metals & Materials Society* 71, 2586–2599. doi:[10.1007/s11837-019-03539-z](https://doi.org/10.1007/s11837-019-03539-z).
- Colas, D., Finot, E., Flouriot, S., Forest, S., Mazière, M., Paris, T., 2021. Experimental and computational approach to fatigue behavior of polycrystalline tantalum. *Metals* 11, 416. doi:[10.3390/met11030416](https://doi.org/10.3390/met11030416).
- Couka, E., Willot, F., Callet, P., Jeulin, D., 2015a. Optical response of a hematite coating: ellipsometry data versus Fourier-based computations. *Advanced Science, Engineering and Medicine* 7, 925–931.
- Couka, E., Willot, F., Jeulin, D., Ben Achour, M., Chesnaud, A., Thorel, A., 2015b. Modeling of the multiscale dispersion of nanoparticles in a hematite coating. *Journal of Nanoscience and Nanotechnology* 15, 3515–3521.
- Decker, L., Jeulin, D., 2000. Simulation 3d de matériaux aléatoires polycristallins. *Revue de Métallurgie* 97, 271–175.
- Delisée, C., Jeulin, D., Michaud, F., 2001. Caractérisation morphologique et porosité en 3d de matériaux fibreux cellulósiques. *Comptes Rendus de l'Académie des Sciences-Series IIB-Mechanics* 329, 179–185.
- Dirrenberger, J., Forest, S., Jeulin, D., 2014. Towards gigantic RVE sizes for 3D stochastic fibrous networks. *International Journal of Solids and Structures* 51, 359–376.
- Duerinckx, M., Gloria, A., Otto, F., 2020. The structure of fluctuations in stochastic homogenization. *Communications in Mathematical Physics* 377, 259–306.
- Egloffé, A.C., Gloria, A., Mourrat, J.C., Nguyen, T.N., 2015. Random walk in random environment, corrector equation and homogenized coefficients: from theory to numerics, back and forth. *IMA journal of numerical analysis* 35, 499–545.
- El Houdaigui, F., Forest, S., Gourgues, A.F., Jeulin, D., 2007a. On the size of the representative volume element for isotropic elastic polycrystalline copper, in: *IUTAM Symposium on Mechanical Behavior and Micro-Mechanics of Nanostructured Materials*. Springer, pp. 171–180.
- El Houdaigui, F., Forest, S., Gourgues, A.F., Jeulin, D., 2007b. Representative volume element sizes for copper bulk polycrystals and thin layer, in: Duparc, O.H. (Ed.), *Colloque 3M Matériaux, Mécanique, Microstructures, sur le thème Interfaces : de l'atome au polycristal*, CEA Saclay / INSTN. pp. 141–153.
- El Moumen, A., Kanit, T., Imad, A., El Minor, H., 2015. Effect of reinforcement shape on physical properties and representative volume element of particles-reinforced composites: statistical and numerical approaches. *Mechanics of materials* 83, 1–16.
- Escoda, J., Willot, F., Jeulin, D., Sanahuja, J., Toulemonde, C., 2011. Estimation of local stresses and elastic properties of a mortar sample by FFT computation of fields on a 3D image. *Cement and Concrete Research* 41, 542–556.

- Escoda, J., Willot, F., Jeulin, D., Sanahuja, J., Toulemonde, C., 2016. Influence of the multiscale distribution of particles on elastic properties of concrete. *International Journal of Engineering Science* 98, 60–71.
- Eyre, D.J., Milton, G.W., 1999. A fast numerical scheme for computing the response of composites using grid refinement. *The European Physical Journal-Applied Physics* 6, 41–47.
- Farooq, H., Cailletaud, G., Forest, S., Ryckelynck, D., 2019. Crystal plasticity modeling of the cyclic behavior of polycrystalline aggregates under non-symmetric uniaxial loading: Global and local analyses. *International Journal of Plasticity* 126, 102619. doi:[10.1016/j.ijplas.2019.10.007](https://doi.org/10.1016/j.ijplas.2019.10.007).
- Figliuzzi, B., Jeulin, D., Faessel, M., Willot, F., Koishi, M., Kowatari, N., 2016. Modelling the microstructure and the viscoelastic behaviour of carbon black filled rubber materials from 3D simulations. *Technische Mechanik* 32, 22–46.
- Fritzen, F., Forest, S., Böhlke, T., Kondo, D., Kanit, T., 2012. Computational homogenization of elasto-plastic porous metals. *International Journal of Plasticity* 29, 102–119. doi:[10.1016/j.ijplas.2011.08.005](https://doi.org/10.1016/j.ijplas.2011.08.005).
- Fritzen, F., Forest, S., Kondo, D., Böhlke, T., 2013. Computational homogenization of porous materials of Green type. *Computational Mechanics* 52, 121–134. doi:[10.1007/s00466-012-0801-z](https://doi.org/10.1007/s00466-012-0801-z).
- Gloria, A., Neukamm, S., Otto, F., 2015. Quantification of ergodicity in stochastic homogenization: optimal bounds via spectral gap on Glauber dynamics. *Inventiones mathematicae* 199, 455–515.
- Hersant, T., Jeulin, D., 1976. L'échantillonnage dans les analyses quantitatives d'images. exemples d'application aux mesures des teneurs de phases dans les agglomérés et des inclusions dans les aciers. *Mémoires et Etudes Scientifiques de la Revue de Métallurgie* 73, 503.
- Hill, R., 1963. Elastic properties of reinforced solids: some theoretical principles. *Journal of the Mechanics and Physics of Solids* 11, 357–372.
- Huet, C., 1990. Application of variational concepts to size effects in elastic heterogeneous bodies. *Journal of the Mechanics and Physics of Solids* 38, 813–841.
- Jean, A., Jeulin, D., Forest, S., Cantournet, S., NGuyen, F., 2011a. A multiscale microstructure model of carbon black distribution in rubber. *Journal of microscopy* 241, 243–260.
- Jean, A., Willot, F., Cantournet, S., Forest, S., Jeulin, D., 2011b. Large-scale computations of effective elastic properties of rubber with carbon black fillers. *International Journal for Multiscale Computational Engineering* 9, 272–303.
- Jeulin, D., 1991a. Modèles de fonctions aléatoires multivariées. *Sci. Terre* 30, 225–256.
- Jeulin, D., 1991b. Modèles Morphologiques de Structures Aléatoires et de Changement d'Echelle. Thèse de Doctorat d'Etat ès Sciences Physiques, Université de Caen.

- Jeulin, D., 2001. Random structure models for homogenization and fracture statistics, in: *Mechanics of random and multiscale microstructures*. Springer, pp. 33–91.
- Jeulin, D., 2005. Space, Structure and Randomness: Contributions in Honor of Georges Matheron in the Field of Geostatistics, Random Sets and Mathematical Morphology, edited by M. Bilodeau, F. Meyer and M. Schmit. Springer New York. chapter Random Structures in Physics. pp. 183–219.
- Jeulin, D., 2012. Morphology and effective properties of multi-scale random sets: A review. *C. R. Mécanique* 340, 219–229.
- Jeulin, D., 2016. Power laws variance scaling of Boolean random varieties. *Methodology and Computing in Applied Probability* 18, 1065–1079.
- Jeulin, D., 2021. *Morphological models of random structures*. Springer.
- Jeulin, D., Moreaud, M., 2008. Statistical representative volume element for predicting the dielectric permittivity of random media, in: *Proceedings CMDS 11*. Les Presses de l’Ecole des Mines de Paris, pp. 429–436.
- Jikov, V.V., Kozlov, S.M., Oleinik, O.A., 1994. *Homogenization of differential operators and integral functionals*. Springer Science.
- Kanit, T., Forest, S., Galliet, I., Mounoury, V., Jeulin, D., 2003. Determination of the size of the representative volume element for random composites: statistical and numerical approach. *International Journal of Solids and Structures* 40, 3647–3679.
- Kanit, T., Forest, S., Jeulin, D., NGuyen, F., Singleton, S., 2011. Virtual improvement of ice cream properties by computational homogenization of microstructures. *Mechanics Research Communications* 38, 136–140.
- Kanit, T., Nguyen, F., Forest, S., Jeulin, D., Reed, M., Singleton, S., 2006. Apparent and effective physical properties of heterogeneous materials: representativity of samples of two materials from food industry. *Computer Methods in Applied Mechanics and Engineering* 195, 3960–3982.
- Koishi, M., Kowatari, N., Figliuzzi, B., Faessel, M., Willot, F., Jeulin, D., 2017. Computational material design of filled rubbers using multi-objective design exploration. *Constitutive Models for Rubber X*; CRC Press: Boca Raton, FL, USA , 467–473.
- Kreher, W., 1990. Residual stresses and stored elastic energy of composites and polycrystals. *Journal of the Mechanics and Physics of Solids* 38, 115–128.
- Kreher, W., Pompe, W., 1985. Field fluctuations in a heterogeneous elastic material-an information theory approach. *Journal of the Mechanics and Physics of Solids* 33, 419–445.
- Kröner, E., 1972. *Statistical continuum mechanics*. volume 92. Springer.
- Laiarinandrasana, L., Jean, A., Jeulin, D., Forest, S., 2012. Modelling the effects of various contents of fillers on the relaxation rate of elastomers. *Materials & Design* 33, 75–82.

- Lantuejoul, C., 1991. Ergodicity and integral range. *Journal of Microscopy* 161, 387–403.
- Madi, K., Forest, S., Jeulin, D., Boussuge, M., 2006. Estimating RVE sizes for 2D/3D viscoplastic composite materials, in: *Matériaux 2006*, Dijon, France.
- Matheron, G., 1965. Les variables régionalisées et leur estimation: une application de la théorie de fonctions aléatoires aux sciences de la nature. volume 4597. Masson Paris.
- Matheron, G., 1967. *Eléments pour une théorie des milieux poreux*. Masson Paris.
- Matheron, G., 1968. Composition des perméabilités en milieu poreux hétérogène: critique de la règle de pondération géométrique. *Rev. IFP* 23, 201–218.
- Matheron, G., 1971. The theory of regionalized variables and its applications. Paris School of Mines publications.
- Matheron, G., 1975. *Random sets and Integral Geometry*. Wiley, New York.
- Matheron, G., 1989. *Estimating and choosing: an essay on probability in practice*. Springer Science & Business Media.
- Matouš, K., Geers, M.G., Kouznetsova, V.G., Gillman, A., 2017. A review of predictive nonlinear theories for multiscale modeling of heterogeneous materials. *Journal of Computational Physics* 330, 192–220.
- Michel, J., Moulinec, H., Suquet, P., 2000. A computational method based on augmented lagrangians and fast Fourier transforms for composites with high contrast. *CMES (Computer Modelling in Engineering & Sciences)* 1, 79–88.
- Moreaud, M., 2006. Propriétés morphologiques multi-échelles et prévision du comportement diélectrique de nanocomposites. Ph.D. thesis. École Nationale Supérieure des Mines de Paris.
- Moulinec, H., Suquet, P., 1994. A fast numerical method for computing the linear and nonlinear mechanical properties of composites. *Comptes Rendus de l'Académie des sciences. Série II. Mécanique, physique, chimie, astronomie* .
- Ostoja-Starzewski, M., 1998. Random field models of heterogeneous materials. *International Journal of Solids and Structures* 35, 2429–2455.
- Oumarou, M., Jeulin, D., Renard, J., 2011. Etude statistique multi-échelle du comportement élastique et thermique d'un composite thermoplastique. *Revue des composites et des matériaux avancés* 21, 221–254.
- Peyrega, C., Jeulin, D., 2013. Estimation of acoustic properties and of the representative volume element of random fibrous media. *Journal of Applied Physics* 113, 104901. doi:[10.1063/1.4794501](https://doi.org/10.1063/1.4794501).
- Ponte Castaneda, P., Willis, J.R., 1988. On the overall properties of nonlinearly viscous composites. *Proceedings of the Royal Society of London. A. Mathematical and Physical Sciences* 416, 217–244.

- Quey, R., Dawson, P., Barbe, F., 2011. Large-scale 3D random polycrystals for the finite element method: Generation, meshing and remeshing. *Computer Methods in Applied Mechanics and Engineering* 200, 1729–1745. doi:[10.1016/j.cma.2011.01.002](https://doi.org/10.1016/j.cma.2011.01.002).
- Sab, K., 1992. On the homogenization and the simulation of random materials. *Eur. J. Mech., A/Solids* 11, 585–607.
- Sanchez-Palencia, E., Zaoui, A., 1987. Homogenization techniques for composite media. volume 272. Springer Science.
- Schneider, M., Josien, M., Otto, F., 2022. Representative volume elements for matrix-inclusion composites—a computational study on the effects of an improper treatment of particles intersecting the boundary and the benefits of periodizing the ensemble. *Journal of the Mechanics and Physics of Solids* 158, 104652.
- Šiška, F., Forest, S., Gumbsch, P., 2007a. Simulation of stress–strain heterogeneities in copper thin films: Texture and substrate effects. *Computational Materials Science* 39, 137–141.
- Šiška, F., Forest, S., Gumbsch, P., Weygand, D., 2007b. Finite element simulations of the cyclic elastoplastic behavior of copper thin films. *Modelling and Simulation in Materials Science and Engineering* 15, S217–S238.
- Suquet, P., Ponte Castaneda, P., 1993. Small-contrast perturbation expansions for the effective properties of nonlinear composites. *Comptes rendus de l’Académie des sciences. Série 2, Mécanique, Physique, Chimie, Sciences de l’univers, Sciences de la Terre* 317, 1515–1522.
- Talbot, D., Willis, J., 1985. Variational principles for inhomogeneous non-linear media. *IMA Journal of Applied Mathematics* 35, 39–54.
- Wiegmann, A., 2007. Computation of the permeability of porous materials from their microstructure by FFF-Stokes. *ITWM Bericht* 129.
- Willis, J., 1982. Elasticity theory of composites, in: *Mechanics of solids*. Elsevier, pp. 653–686.
- Willis, J., 1991. On methods for bounding the overall properties of nonlinear composites. *Journal of the Mechanics and Physics of Solids* 39, 73–86.
- Willis, J., 2001. Lectures on mechanics of random media, in: *Mechanics of random and multiscale microstructures*. Springer, pp. 221–267.
- Willot, F., Abdallah, B., Jeulin, D., 2016. The permeability of Boolean sets of cylinders. *Oil & Gas Science and Technology—Revue d’IFP Energies nouvelles* 71, 52.
- Willot, F., Gillibert, L., Jeulin, D., 2013. Microstructure-induced hotspots in the thermal and elastic responses of granular media. *International Journal of Solids and Structures* 50, 1699–1709.
- Willot, F., Jeulin, D., 2009. Elastic behavior of composites containing Boolean random sets of inhomogeneities. *International Journal of Engineering Sciences* 47, 313–324.
- Willot, F., Jeulin, D., 2011. Elastic and electrical behavior of some random multiscale highly-contrasted composites. *International Journal of Multiscale Computational Engineering* 9, 305–326.

- Willot, F., Pellegrini, Y., 2008. Fast Fourier transform computations and build-up of plastic deformation in 2d, elastic-perfectly plastic, pixelwise disordered porous media, in: Proceedings CMDS 11. Les Presses de l'Ecole des Mines de Paris, pp. 442–449.
- Zeghadi, A., Forest, S., Gourgues, A.F., Bouaziz, O., 2007a. Ensemble averaging stress–strain fields in polycrystalline aggregates with a constrained surface microstructure—Part 2: Crystal plasticity. *Philosophical Magazine* 87, 1425–1446. doi:[10.1080/14786430601009517](https://doi.org/10.1080/14786430601009517).
- Zeghadi, A., Nguyen, F., Forest, S., Gourgues, A.F., Bouaziz, O., 2007b. Ensemble averaging stress–strain fields in polycrystalline aggregates with a constrained surface microstructure—Part 1: Anisotropic elastic behaviour. *Philosophical Magazine* 87, 1401–1424. doi:[10.1080/14786430601009509](https://doi.org/10.1080/14786430601009509).